J|A|C|S ARTICLES

Published on Web 07/22/2010

A Tyrosyl−Dimanganese Coupled Spin System is the Native Metalloradical Cofactor of the R2F Subunit of the Ribonucleotide Reductase of *Corynebacterium ammoniagenes*

Nicholas Cox,*,† Hideaki Ogata,† Patrick Stolle,‡ Edward Reijerse,† Georg Auling,‡ and Wolfgang Lubitz*,†

Max-Planck-Institut für Bioanorganische Chemie, Stiftstrasse 34-36, D-45470 Mülheim (Ruhr), Germany, and Institut für Mikrobiologie, Leibniz Universität Hannover, Schneiderberg 50, D-30167 Hannover, Germany

Received April 30, 2010; E-mail: cox@mpi-muelheim.mpg.de; lubitz@mpi-muelheim.mpg.de

Abstract: The X-ray crystallographic structure of the native R2F subunit of the ribonucleotide reductase (RNR) of *Corynebacterium ammoniagenes* ATCC 6872 is reported, with a resolution of 1.36 Å. The metal site contains an oxo/hydroxo-bridged manganese dimer, located near a tyrosine residue (Y115). The coordination of the manganese dimer and its distance to a nearby tyrosine residue resemble the di-iron metalloradical cofactor of class I RNR from *Escherichia coli*. Multifrequency EPR measurements of the highly active *C. ammoniagenes* R2F subunit show that the metal site contains a ferromagnetically exchange-coupled $Mn^{III}Mn^{III}$ dimer weakly coupled to a tyrosyl radical. A mechanism for the metalloradical cofactor ($Mn^{III}Mn^{III}Y^{\bullet}$) generation is proposed. H_2O_2 (HO_2^-) instead of O_2 is hypothesized as physiological oxidant for the Mn dimer which in turn oxidizes the tyrosine Y115. Changes in the ligand sphere of both manganese ions during metalloradical generation direct the complex formation of this cofactor, disfavoring alternate reaction pathways such as H_2O_2 dismutation, as observed for manganese catalase, a structural analogue of the R2F metal site. The presented results demonstrate the importance of manganese for radical formation in this RNR and confirm the assignment of this enzyme to class Ib.

1. Introduction

Deoxyribonucleic acid (DNA)—nature's universal information storage medium—is synthesized from deoxyribonucleotide monomers, which are provided by a single enzyme, ribonucleotide reductase (RNR), in all organisms.[1,2] Ribonucleotide substrate conversion occurs via a radical reaction mechanism that is highly conserved.[3] The currently accepted reaction pathway is initiated by a distant radical species and involves the sequential activation of a cysteine or a glycine to facilitate deoxygenation of the ribonucleotide via hydrogen abstraction and water release.[1,4]

Class I RNR consists of two homodimeric proteins, a larger subunit R1 that contains the catalytic site and the binding site for allosteric effectors and a smaller subunit R2 that harbors the metalloradical cofactor, a ferric di-iron cluster that stabilizes a free tyrosyl radical,[2,5,6] the distant radical species that initiates cysteine activation i.e. enzymatic function. Class I is further divided into: class Ia, encoded by the *nrdAB* genes and class Ib, encoded by *nrdE* (R1E) and *nrdF* (R2F). A third subclass, class Ic was established for the tyrosyl radical lacking *Chlamydia trachomatis* RNR.[7−10] Both class Ia and Ib are expressed in *E. coli*. In *E. coli*, class Ib RNR is up-regulated under stress conditions including Fe starvation and oxidative stress;[11−13] the exogenous addition of H_2O_2 increases the expression of class Ib RNR.

The native RNR of the Gram-positive bacterium *Corynebacterium ammoniagenes* shares many of the characteristics of class Ib RNRs: oxygen sensitivity, genetic encoding, behavior toward reductant—in particular NrdH-redoxins, which are characterized by a glutaredoxin-like amino acid sequence but show a thioredoxin-like activity profile.[14−17] In addition, the R2F subunit of RNR from *C. ammoniagenes* has been shown to be

† Max-Planck-Institut für Bioanorganische Chemie.
‡ Institut für Mikrobiologie, Leibniz Universität Hannover.

(1) Follmann, H. *Chem. Soc. Rev.* **2004**, *33*, 225–233.
(2) Sjöberg, B. In *Metal Sites in Proteins and Models*; Allen, H., Hill, O., Sadler, P. J., Thomson, A. J., Eds.; Structure and Bonding, Vol. Springer-Verlag: Berlin, 1997; pp 139−173.
(3) Reichard, P. *Science* **1993**, *260*, 1773–1777.
(4) Stubbe, J.; Nocera, D. G.; Yee, C. S.; Chang, M. C. *Chem Rev* **2003**, *103*, 2167–201.
(5) Nordlund, P.; Sjöberg, B.; Eklund, H. *Nature* **1990**, *345*, 593–598.
(6) Uhlin, U.; Eklund, H. *Nature* **1994**, *370*, 533–539.
(7) Jiang, W.; Yun, D.; Saleh, L.; Barr, E. W.; Xing, G.; Hoffart, L. M.; Maslak, M.-A.; Krebs, C.; Bollinger, J. M., Jr. *Science* **2007**, *316*, 1188–1191.
(8) Voevodskaya, N.; Lendzian, F.; Ehrenberg, A.; Gräslund, A. *FEBS Lett.* **2007**, *581*, 3351–3355.
(9) Voevodskaya, N.; Narvaez, A.-J.; Domkin, V.; Torrents, E.; Thelander, L.; Gräslund, A. *Proc. Natl. Acad. Sci. U.S.A.* **2006**, *103*, 9850–9854.
(10) Högbom, M.; Stenmark, P.; Voevodskaya, N.; McClarty, G.; Gräslund, A.; Nordlund, P. *Science* **2004**, *305*, 245–248.
(11) McHugh, J. P.; Rodriguez-Quinones, F.; Abdul-Tehrani, H.; Svistunenko, D. A.; Poole, R. K.; Cooper, C. E.; Andrews, S. C. *J. Biol. Chem.* **2003**, *278*, 29478–29486.
(12) Monje-Casas, F.; Jurado, J.; Prieto-Ãlamo, M.-J.; Holmgren, A.; Pueyo, C. *J. Biol. Chem.* **2001**, *276*, 18031–18037.
(13) Vassinova, N.; Kozyrev, D. *Microbiology* **2000**, *146*, 3171–3182.

structurally similar to class Ib RNR sourced from *Salmonella typhimurium*, which has thus far been described as a di-iron enzyme.[18,19] However, unlike class I RNRs *C. ammoniagenes* appears to require manganese instead of iron for enzymatic function.[14,20]

The precise function of cellular manganese in *C. ammoniagenes* remains an open question. Manganese deprivation[21] of *C. ammoniagenes* leads to a reduced DNA content, suggesting the native RNR uses manganese instead of iron for metalloradical cofactor assembly.[14,22,23] Studies of Griepenburg et al.[24,25] supported the notion that the R2F subunit did indeed display properties divergent from that of class Ia, RNR. However, this contrasted with the first crystal structure of the R2F subunit, reported by Högbom et al.[26] Here the cloned *nrdF* gene of *C. ammoniagenes* was heterologously expressed in *E. coli*, and the isolated apo-R2F subunit was subsequently reactivated with Fe^{II} ascorbate *in vitro*. When prepared under aerobic conditions, the R2F subunit contained a μ-oxo-bridged $Fe^{III}Fe^{III}$ metallocofactor analogous to that observed for *E. coli* class Ia RNR. This led these authors to propose a di-iron metalloradical cofactor.[15,27]

The crystallographic results described above are in conflict with experiments performed in the native system. Homologous expression of R2F sourced from *C. ammoniagenes* ATCC 6872, the strain from which the enzyme was originally isolated,[14] does not show any significant iron incorporation into the enzyme. Similarly, iron-substituted RNR displays a significantly lower activity when compared to the native enzyme, which has turnover rates comparable to that of the RNR of *E. coli*.[28] These results suggest that in vitro metal reconstitution as described above may lead to incorrect metal incorporation into this metalloprotein.

Recently, a highly active Mn-RNR was obtained as a native protein from a wild type strain of *C. glutamicum* with a distinct tyrosyl radical.[29] The genome of this amino acid producer harbors only *nrdEF* genes,[30] and its DNA content is reduced under Mn deprivation (unpublished results). Similarly, ribonucleotide reduction, but not DNA replication, is impaired by manganese deprivation in related bacteria of the genus *Arthrobacter*.[31]

The role of Mn as an integral component of the native metalloradical cofactor of all class Ib RNRs has recently been raised by Cotruvo and Stubbe.[32] These authors have shown that the usually inactive class Ib enzyme of *E. coli* can be activated by Mn using apo-R2F and an additional flavodoxin (NrdI) encoded by the *nrdI* gene. This additional protein may be common to all class Ib enzymes.[32] They propose that the role of the NrdI in metalloradical cofactor biosynthesis is to provide oxidizing equivalents (H_2O_2, HO_2^-, etc.), derived from O_2,[33] to the reduced Mn complex. This would then suggest that cofactor assembly in part resembles the Mn catalase H_2O_2 dismutation reaction pathway.[34−36] They also note that the same protein can assemble an Fe metalloradical cofactor albeit with lower enzyme activity. In this light, it is conceivable that Mn, not Fe, may be the native metal used *in vivo* by all class Ib RNRs.

Here we present new spectroscopic and crystallographic data on native-type R2F from *C. ammoniagenes* ATCC 6872. These measurements show conclusively that the metalloradical cofactor contains a μ-oxo/hydroxo-bridged manganese dimer, with a structure very similar to that of the di-iron complex of *E. coli* R2 in its oxidized, active form. Spectral simulations of the metalloradical cofactors' EPR signal observed at 9, 34, and 244 GHz suggest that the two manganese centers are ferromagnetically exchange-coupled, and interact weakly with the nearby tyrosyl radical. These findings underline the important role of the manganese for the radical formation in this unusual RNR and support the current assignment of RNR derived from *C. ammoniagenes* to class Ib.

2. Materials and Methods

2.1. Purification of the Native R2F Subunit. *C. ammoniagenes* pOCA2 was grown aerobically at 27 °C in LB medium with chloramphenicol (15 μg/mL) in a 10-L New Brunswick bioreactor (aeration 8 L/min; agitation 350 rpm). The *nrdF* gene was induced by addition of 0.6 mM isopropyl-β-D-thiogalactopyranoside (IPTG) and 185 μM $MnCl_2$ or $Fe(NH_4)_2$-citrate in the midlogarithmic growth phase at an OD_{600} of 7. After 4 h, maximal R2F biosynthesis was reached, as observed by SDS-PAGE and Western blotting. The culture was rapidly cooled down to 4 °C and was kept at this temperature during all further operations. Sixty grams of cells (wet weight) were harvested by centrifugation and resuspended in a buffer containing 85 mM phosphate, 100 mM KCl, 2 mM dithiothretiol (DTT), 0.1% Tween 80 (pH 6.6). The cells were disrupted by three passages in a French Press at 1500 psi. R2F precipitated in the range of 40−60% ammonium sulfate saturation. Salts were removed using HiTrap desalting columns and standard buffer (85 mM phosphate buffer, pH 6.6, 2 mM DTT) prior to enrichment by ion-exchange chromatography (IEC) using a three-step gradient and a Unosphere Q column. The R2F subunit eluted at 350 mM KCl (standard buffer including 1 M KCl) and was submitted to size exclusion chromatography (SEC) using Superdex

(14) Willing, A.; Follmann, H.; Auling, G. *Eur. J. Biochem.* **1988**, *175*, 167–173.
(15) Fieschi, F.; Torrents, E.; Toulokhonova, L.; Jordan, A.; Hellman, U.; Barbe, J.; Gibert, I.; Karlsson, M.; Sjöberg, B.-M. *J. Biol. Chem.* **1998**, *273*, 4329–4337.
(16) Oehlmann, W.; Griepenburg, U.; Auling, G. *Biotechnol. Lett.* **1998**, *20*, 483–488.
(17) Stehr, M.; Lindqvist, Y. *Proteins* **2004**, *55*, 613–619.
(18) Eriksson, M.; Jordan, A.; Eklund, H. *Biochemistry* **1998**, *37*, 13359–13369.
(19) Jordan, A.; Pontis, E.; Atta, M.; Krook, M.; Gibert, I.; Barbe, J.; Reichard, P. *Proc. Natl. Acad. Sci. U.S.A.* **1994**, *91*, 12892–12896.
(20) Auling, G.; Follmann, H. In *Metal Ions in Biological Systems*; Sigel, H., Sigel, A., Eds.; Marcel Dekker Inc: New York, 1994; Vol. 30, pp 132−161.
(21) Oka, T.; Udagawa, K.; Kinoshita, S. *J. Bacteriol.* **1968**, *96*, 1760–1767.
(22) Auling, G.; Thaler, M.; Diekmann, H. *Arch. Microbiol.* **1980**, *127*, 105–114.
(23) Schimpff-Weiland, G.; Follmann, H.; Auling, G. *Biochem. Biophys. Res. Commun.* **1981**, *102*, 1276–1282.
(24) Griepenburg, U.; Lassmann, G.; Auling, G. *Free Radical Res.* **1996**, *24*, 473–481.
(25) Griepenburg, U.; Blasczyk, K.; Kappl, R.; Hüttermann, J.; Auling, G. *Biochemistry* **1998**, *37*, 7992–6.
(26) Högbom, M.; Huque, Y.; Sjöberg, B.-M.; Nordlund, P. *Biochemistry* **2002**, *41*, 1381–1389.
(27) Huque, Y.; Fieschi, F.; Torrents, E.; Gibert, I.; Eliasson, R.; Reichard, P.; Sahlin, M.; Sjöberg, B. M. *J. Biol. Chem.* **2000**, *275*, 25365–25371.
(28) Stolle, P.; Barckhausen, O.; Oehlmann, W.; Knobbe, N.; Vogt, C.; Pierik, A.; Schmidt, P.; Reijerse, E.; Lubitz, W.; Auling, G. *FEBS Journal.* **2010**, submitted.
(29) Abbouni, B.; Oehlmann, W.; Stolle, P.; Pierik, A. J.; Auling, G. *Free Radical Res.* **2009**, 1–8.
(30) Kalinowski, J.; et al. *J. Biotechnol.* **2003**, *104*, 5−25.
(31) Plönzig, J.; Auling, G. *Arch. Microbiol.* **1987**, *146*, 396–401.
(32) Cotruvo, J. A.; Stubbe, J. *Biochemistry* **2010**, *49*, 1297–1309.
(33) Massey, V. *J. Biol. Chem.* **1994**, *269*, 22459–22462.
(34) Dismukes, G. C. *Chem. Rev.* **1996**, *96*, 2909–2926.
(35) Boelrijk, A. E. M.; Dismukes, G. C. *Inorg. Chem.* **2000**, *39*, 3020–3028.
(36) Barynin, V. V.; Whittaker, M. M.; Antonyuk, S. V.; Lamzin, S. V.; Harrison, P. M.; Artymiuk, A. J.; Whittaker, J. M. *Structure* **2001**, *9*, 725–738.

Table 1. X-ray Data Collection Statistics and Refinement Statistics[a]

	native	Mn_{peak}
Data Collection		
X-ray source	BL41XU at SPring-8	BL41XU at SPring-8
wavelength (Å)	1.00000	1.89000
space group	*C*2	*C*2
unit-cell parameters		
a, *b*, *c* (Å)	96.21, 87.68, 83.25	95.97, 87.55, 83.29
α, *β*, *γ* (deg)	90.00, 99.29, 90.00	90.00, 99.36, 90.00
resolution (Å)	31.17−1.36 (1.41−1.36)	33.01−1.84 (1.91−1.84)
no. of observed reflections	502993	206100
no. of unique reflections	140012	58827
R_{merge}	0.073 (0.477)	0.077 (0.341)
completeness (%)	96.1 (72.7)	99.7 (100.0)
$\langle I/\sigma(I)\rangle$	13.4 (2.1)	28.4 (4.1)
redundancies	3.6	3.5
Refinement		
no. of reflections used in refinement	132961	
resolution used in refinement	20.0−1.36	
R	0.164	
R_{free}	0.210	
rms deviation		
bonds (Å)	0.010	
angles (deg)	0.026	
no. of protein atoms	4838	
no. of water molecules	606	

[a] Values in parentheses are for the highest resolution shell.

200. R2F was solely recovered in the 32−45 kDa fractions as assessed by SDS-PAGE and Western blot with anti-R2F antibody. The R2F-positive fractions were adsorbed to a Mono Q HR 5/5 column, eluted in the range of 520−535 mM KCl using a linear gradient and concentrated using Amicon Ultra-4 centrifugal devices (cut off 10 kDa). Further details of the molecular biological and biochemical protocol are described elsewhere, by Stolle et al.[28] Metal quantification was performed using: (i) graphite furnace atomic absorption spectroscopy (GF-AAS), (ii) inductively coupled plasma mass spectrometry (ICPMS), and (iii) by oxidation of the bound Mn to MnO_4^-.[28] The enzyme activity was determined according to ref 37.

2.2. Crystallographic Analysis of the R2F Protein. The purified R2F protein solution was concentrated to 10 mg·mL^{-1}. Crystallization was carried out using the sitting-drop vapor diffusion method at 277 K under aerobic condition. Crystals suited for diffraction experiments required a buffering medium that included: 0.1 M sodium citrate, 27.5% PEG4000, 0.05 M ammonium acetate pH 6.0, and 0.1 M ammonium acetate pH 7.0, with 0.05 M Tris/HCl pH 7.5. All data sets were collected at 100 K using the BL41XU beamline at SPring-8 (Hyogo, Japan). The detector used was a MX225HE (MAR research, Germany). The data sets were indexed, integrated, and scaled using the program HKL2000.[38] The molecular replacement and the initial refinement of the structure were carried out using the program CCP4 and REFMAC, respectively.[39] As coordinates for the search model, the data from R2F from *C. ammoniagenes* (PDB ID 1kgp) was used. Model building and final refinement were performed using WINCOOT and SHELX-97.[40,41] The experimental conditions are summarized in Table 1. XRF experiments for determination of the metal composition of R2F were carried out using the BL14.2 beamline at BESSY II (Berlin, Germany). A preliminary report was published in ref 42.

2.3. Multifrequency EPR Measurements. X-band spectra (9.4 GHz) were recorded with a Bruker Elexsys E500 spectrometer equipped with an Oxford Instruments ESR-910 helium flow cryostat. The samples were contained in quartz tubes of 4 mm outer diameter. Q-band spectra (34.0 GHz) were recorded with a Bruker ESP300E EPR spectrometer equipped with an Oxford instruments CF935 helium flow cryostat and a standard Bruker ER5106QT resonator. Q-band samples were contained in 3 mm quartz tubes. High-field EPR measurements at 244 GHz were recorded using a home-built quasi-optical EPR spectrometer described in ref 43. The CW EPR spectra were recorded at 5 K in a nonresonant Teflon sample holder containing 20 μL of 1 mM protein solution. Approximately 5 mW microwave power was available at 244 GHz leading to partial saturation of the radical signal such that a "passage" (absorption-like) line shape was obtained. The recorded spectra were pseudomodulated to obtain the derivative mode line shape presented in Figure 11. The magnetic field axis was calibrated using a Mn(II)/MgO standard.[44]

EPR signals observed at 9, 34, and 244 GHz were simultaneously fit assuming a three-spin model (see Theory). The calculations assumed that all tensors were colinear. Spectral simulations were performed numerically using Scilab-4.4.1, an open source vector-based linear algebra package (www.scilab.org) and the easyspin package[45] in MATLAB.

3. Theory

3.1. The Spin Hamiltonian Formalism 1: A General Model. Here we consider an exchange coupled Mn dimer (Mn_A-Mn_B) weakly coupled to an organic radical R with $S = {}^1/_2$. The precise oxidation states of the two Mn are unknown but are limited to three states: Mn^{II} ($S = {}^5/_2$), Mn^{III} ($S = 2$) or Mn^{IV} ($S = {}^3/_2$). As a consequence, there are five different oxidation state combinations the Mn dimer can take: $Mn^{II}Mn^{II}$, $Mn^{II}Mn^{III}$, $Mn^{III}Mn^{III}$, $Mn^{III}Mn^{IV}$, $Mn^{IV}Mn^{IV}$.

A basis set that describes the Mn-dimer−radical ($R^\bullet$, $S_R = {}^1/_2$) spin manifold can be built from the product of the eigenstates of the three interacting spins:

$$|S_A S_B S_R m_A m_B m_R\rangle \tag{1}$$

Here S_A, S_B and S_R refer to the electronic spin state of Mn_A, Mn_B and S_R; m_A, m_B and m_R refer to the magnetic sublevels of each spin. m_X takes values S_X, S_X-1, ..., $1-S_X$, S_X (where $X =$ A, B, R). S_A and S_B can take values 1, ${}^3/_2$, and 2, depending on the oxidation state of the Mn dimer. S_R is always ${}^1/_2$. Thus, the model describing a $Mn^{II}Mn^{II}$ dimer interacting with a radical requires 72 basis vectors, the $Mn^{III}Mn^{III}-R^\bullet$ model requires 50 basis vectors and the $Mn^{IV}Mn^{IV}-R^\bullet$ model requires only 32 basis vectors.

The spin Hamiltonian appropriate to describe our system can be written as

(37) Willing, A.; Follmann, H.; Auling, G. *Eur. J. Biochem.* **1988**, *170*, 603–611.
(38) Otwinowski, Z.; Minor, W. *Methods Enzymol.* **1997**, *276*, 307–326.
(39) Collaborative Computational Project, N. *Acta Crystallogr., Sect. D* **1994**, 50.
(40) Emsley, P.; Cowtan, K. *Acta Crystallogr., Sect. D* **2004**, 60.
(41) Sheldrick, G. M. *Acta Crystallogr., Sect. A* **2008**, 64.
(42) Ogata, H.; Stolle, P.; Stehr, M.; Auling, G.; Lubitz, W. *Acta Crystallogr., Sect. F* **2009**, *65*, 878–880.
(43) Reijerse, E.; Schmidt, P.; Klihm, G.; Lubitz, W. *Appl. Magn. Reson.* **2007**, *31*, 611–626.
(44) Burghaus, O.; Rohrer, M.; Goetzinger, T.; Plato, M.; Moebius, K. *Meas. Sci. Technol.* **1992**, *3*, 765–774.
(45) Stoll, S.; Schweiger, A. *J. Magn. Reson.* **2006**, *178*, 42–55.

$$H = \sum_{i=\mathrm{A,B}} (D_i[(S_{iZ}^2 - {}^1/_3 S_i(S_i+1) + {}^{E_i}/_{D_i}(S_{iX}^2 - SX_{iY}^2)] + \beta B \cdot g_{\mathrm{Mn}_i} \cdot S_i - S_i \cdot J_{\mathrm{Int}_i} \cdot S_\mathrm{R}) - S_\mathrm{A} \cdot J \cdot S_\mathrm{B} + \beta B \cdot \mathrm{g}_\mathrm{R} \cdot S_\mathrm{R} \quad (2)$$

Here all nuclear hyperfine and quadrupole terms of magnetic nuclei (e.g., ^{55}Mn) have been excluded since they are small and only contribute to the fitted line width. The spin Hamiltonian includes three coupling tensors that describe the interaction between the two Mn and the interaction between each Mn and the tyrosyl radical; three Zeeman tensors (**g**), one for each spin center; and two fine structure tensors, one for each Mn.

3.2. The Coupling Tensors $S_\mathrm{A}\cdot J\cdot S_\mathrm{B}$ and $S_i \cdot J_\mathrm{int}\cdot S_\mathrm{R}$. The coupling tensors $S_\mathrm{A}\cdot J\cdot S_\mathrm{B}$ and $S_i \cdot J_\mathrm{int}\cdot S_\mathrm{R}$ (where i = A, B) include all isotropic and anisotropic interactions between the two spins. The first tensor, the Mn−Mn interaction is expected to be large and dominated by the exchange coupling term. In most systems it is sufficient to treat this interaction as isotropic i.e. $JS_1\cdot S_2$. In contrast, the two Mn−radical interactions are expected to be small. Here both exchange (through bond) and dipolar (through space) mechanisms contribute to the interaction. The Mn−radical interaction tensor can be decomposed into two parts (J_iso, J_aniso)

$$S_i \cdot J_\mathrm{int} \cdot S_\mathrm{R} = J_\mathrm{iso} S_i \cdot S_\mathrm{R} + S_i \cdot J_\mathrm{aniso} \cdot S_\mathrm{R} \quad (3)$$

In general the anisotropic term has both exchange and dipolar contributions. However, it is usually sufficient to ignore the exchange component of this term and assume the anisotropic interaction is dominantly derived from the through space dipolar interaction between the two spins:

$$S_i \cdot J_\mathrm{aniso} \cdot S_\mathrm{R} \approx S_i \cdot d_\mathrm{dip} \cdot S_\mathrm{R} \quad (4a)$$

$$S_i \cdot d_\mathrm{dip} \cdot S_\mathrm{R} = g_i g_\mathrm{R} \beta^2 [S_{iX} \;\; S_{iY} \;\; S_{iZ}] \cdot \begin{bmatrix} -\frac{2}{r^3} & 0 & 0 \\ 0 & \frac{1}{r^3} & 0 \\ 0 & 0 & \frac{1}{r^3} \end{bmatrix} \cdot \begin{bmatrix} S_{RX} \\ S_{RY} \\ S_{RZ} \end{bmatrix} \quad (4b)$$

Here r represents the distance between the two spin centers. The traceless dipole−dipole tensor (d_dip) as shown above is written such that the interspin vector is aligned along the X axis. Canonical rotation realigns the interspin vector along Y or Z. A nondiagonal dipole−dipole tensor is observed for an arbitrary interspin vector orientation.

For all the simulations presented in the manuscript the full coupling tensor J_int with components ($J_{\mathrm{int}x}$, $J_{\mathrm{int}y}$, $J_{\mathrm{int}z}$) was used. The isotropic component of the coupling tensor was not treated as a separate variable, nor was the coupling tensor assumed to be axially symmetric.

3.3. Split-Radical Signals. A 'Split-Radical' signal, as seen in EPR, is observed when a radical is weakly coupled to another paramagnetic center. The interaction has to be of the order of the radical's line width i.e. ~100 MHz. The split radical signal can be considered, to zeroth order, as an isolated radical that is perturbed by its interaction with a nearby paramagnetic center. An important subset of split radical signals is that where the radical interacts with a metal center. Metal centers typically have large inhomogeneous linewidths associated with **g** and hyperfine anisotropy as compared to radical signals, which are generally not broader than 100 MHz. For most orientations–specific sites within the metal signal envelope–the coupling between the metal and the radical is small relative to the difference in g-value ($J \ll \Delta g$), i.e. we are in the weak coupling limit.[46] The sum over all orientations yields a 'splitting' of the radical signal and a broader metal site distribution that may or may not resolve a splitting. The split radical signal pattern for a radical interacting with a $S = {}^1/_2$ metal center is shown in Figure 1.

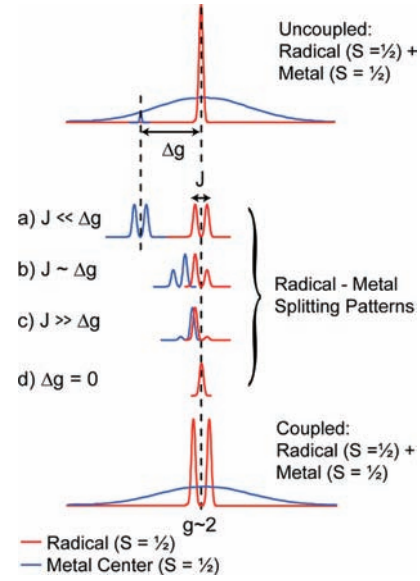

Figure 1. A pictorial representation of a S = ½ radical weakly interacting with a S = ½ metal ion. The top trace shows the uncoupled radical-metal signal. Metals characteristically have large inhomogeneous EPR linewidths due to large g and hyperfine anisotropy as compared to organic radicals. As represented in figure 1, unresolved g and hyperfine anisotropy broaden the EPR lineshape of the metal significantly, resulting in a structureless signal centered at g~2. The radical-metal interaction depends on which component of the metal's inhomogeneous line the radical interacts with. For most orientations (specific sites within the metal signal envelope) the coupling between the metal and the radical is small relative to the difference in g-value ($J \ll \Delta g$). In this case, the radical and metal signals split about their uncoupled g-positions, with each peak approximately having the same intensity (a). As the Δg decreases relative to J, a more complicated coupled signal pattern emerges (b and c). The intensity of the four peaks is redistributed such that the outer peaks' (satellites) intensity decreases relative to the center peaks. The powder spectrum observed is the sum of all these interaction types. For a sufficiently broad metal signal, the weak coupling limit ($J \ll \Delta g$) dominates. Its CW EPR spectrum resolves a 'splitting' of the radical signal and a broader metal site distribution that may or may not resolve a splitting. Although a Gaussian lineshape is assumed for the EPR signal of the metal ion, the same arguments are applicable for any arbitrary lineshape.

The number of 'splittings'–spectral lines of the split radical pattern centered about $g \approx 2.0$–corresponds to the number of discrete magnetic sublevels (m_S sublevels) the metal system contains. For instance, a $S = 2$ metal contains five m_S sublevels (Figure 2). When weakly coupled to a radical, the radical line splits into five spectral lines. The low- and high-field edges of the split radical signal are defined by the radical's interaction with the $|m_S| = 2$ sublevels. The radical's interaction with $|m_s| = 1$ sublevels appear toward the center of the split-pattern. The coupling of the radical to the $m_S = 0$ sublevel results in no perturbation of the radical. The line separation within the split-pattern is equal to the metal−radical coupling J, for an isotropic

(46) Carrington, A.; McLachlan, A. D. *Introduction to Magnetic Resonance*, 1st ed.; Harper and Row: New York, 1967.

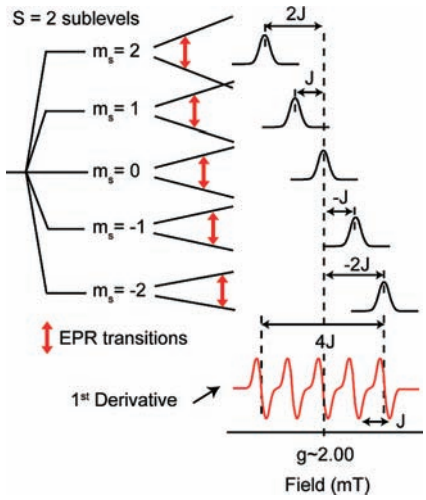

Figure 2. 'Split-radical' pattern observed in CW EPR for a $S = {}^1/_2$ radical coupled to a metal center of $S = 2$. Five transitions are observed, corresponding to the interaction of the radical with each of the electronic sublevels of the metal. The low- and high-field lines are defined by the radical's interaction with the $|m_s| = 2$ sublevels. The first derivative EPR spectrum resolves five features: four lines are observed about an unperturbed central line. The central line is derived from the interaction of the radical with the $m_s = 0$ sublevel of the metal center. The separation of the lines in the first derivative spectrum (red) is equal to J.[46]

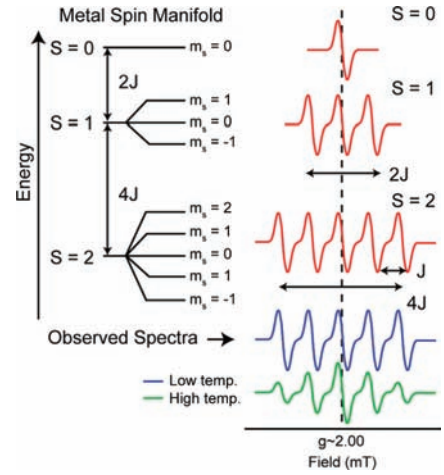

Figure 3. 'Split-radical' pattern observed in CW EPR for a $S = {}^1/_2$ radical coupled to a metal spin manifold with ground state $S = 2$. At low temperatures, only the ground state of the spin manifold is populated and the EPR spectrum shows only the radical interacting with an $S = 2$ spin. As the temperatures is increased, higher spin states of the metal spin manifold are populated, namely $S_T = 1$ and $S_T = 0$. The ground state in a ferromagnetically coupled dimer will always have the highest effective spin (S_T) as compared to all the other spin manifold states and thus its interaction with a radical will yield the broadest contribution to the observed EPR signal.

metal−radical interaction and thus the total spectral breadth of this signal is $4J$ (Figure 2). This represents a general result for all split-radical signals. The observation that the coupling of a radical to the $m_S = 0$ sublevel of the metal spin manifold does not affect the position and shape of its signal provides one way to discriminate between different metal−radical interactions. The interaction of a radical with a half-integer spin metal (i.e., Mn^{IV}, $S = {}^3/_2$) should not contain an unperturbed central line at $g \approx 2$, whereas its interaction with an integer spin metal (i.e., Mn^{III}, $S = 2$) should.

The spin manifold of a coupled spin system can contain more than one contribution. Higher spin states can also add to the observed split-radical signal pattern. This is shown in Figure 3 for a ferromagnetically coupled $S_T = 2$ spin manifold. At low temperatures, only the ground state of the spin manifold is populated and the EPR spectrum shows only the radical interacting with an $S = 2$ spin. As the temperature is increased, the spectrum may also contain contributions from higher spins states, in this instance $S_T = 1$ and $S_T = 0$. These add intensity to the center of the pattern. The ground state in a ferromagnetically coupled dimer will always have the highest effective spin (S_T) as compared to all the other spin manifold states and thus its interaction with a radical will yield the broadest contribution to the observed EPR signal.[47] The opposite is observed for an antiferromagnetically coupled dimer. Here the ground state contribution to the EPR spectrum will be the narrowest component. The magnitude of the exchange coupling within the metal spin system dominantly determines the ladder spacing of the manifold and as a consequence, the temperature dependence of the split radical signal. In the case of a Mn dimer, the exchange coupling (J) between the two metal centers has to be of the order of the microwave quantum for the split-radical signal to show any significant temperature dependence at cryogenic temperatures (5−30 K).

(47) The splitting to first order is expected to scale with S_T, splitting $= 2J_{int}S_TS_R = 2J_{int}{}^1/_2S_T = J_{int}S_T$. As the ground spin multiplet has the largest total spin, it defines the edges of the signal envelope.

The energy levels of the metal/metal system, as shown in Figures 2 and 3, assume that the Zeeman term is the dominant term in the spin Hamiltonian. In this case the eigenstates of the metal can be assumed to be the unperturbed basis set to a good approximation, i.e. for $S = 2$, the eigenstates for a single metal are: $|2,2\rangle$, $|2,1\rangle$,$|2,0\rangle$, $|2,-1\rangle$,$|2,-2\rangle$. Mn^{III} and Mn^{IV} typically have zero-field splittings of $\sim 1\ cm^{-1}$. This is of the order of the microwave quanta (Zeeman term) at X ($\sim 0.3\ cm^{-1}$)- and Q ($\sim 0.9\ cm^{-1}$)-bands. Here the eigenstates of the system are mixed, such that the ladder of states as presented in Figure 2 is no longer valid. However, in this case the same key observations still apply, namely (i) the number of lines in the split signal pattern is still dependent on the number of energy levels the metal/metal system contains, and (ii) the spectral breadth of the split radical signal is defined by the metal−radical coupling interaction. The effect of the on site zero-field splitting of the metal is to redistribute signal intensity within the split-radical pattern. This effect can also lead to a norrowing of the spilt-radical pattern.

3.4. The Spin Hamiltonian Formalism 2: A Simplified Model. It is observed that the split radical signal is derived from only one component of the total spin manifold (Figure 1) and as such is only sensitive to specific elements of the above spin Hamiltonian, in particular those that involve the spin operator S_R. These include the Mn−radical exchange terms and at high field, the intrinsic **g**-tensor of the radical. Terms that only include the S_A and S_B operators are less well defined. For instance the Mn g-anisotropy is shown to have little effect on the split radical signal and can be approximated by a single isotropic value. This allows us to use a simpler Hamiltonian outlined below to ensure the derived solution is unique.

$$H = \sum_{i=A,B} (D_i[(S_{iZ}^2 - {}^1/_3S_i(S_i + 1) + {}^{E_i}/_{D_i}(S_{iX}^2 - S_{iY}^2)] + g_{Mn}\beta B \cdot S_i - S_i \cdot J_{Int} \cdot S_R) - JS_A \cdot S_B + \beta B \cdot g_R \cdot S_R \quad (5)$$

Here both g_{Mn} and $\mathbf{J_{int}}$ are assumed to be the same for both Mn centers to limit the size of the parameter set.

4. Results

4.1. Biochemical Assay.

4.1.1. Characterization of the Native-Type R2F from *C. ammoniagenes.* To improve R2F synthesis yields, a second, cloned *nrdF* gene from *C. ammoniagenes* ATCC 6872[16] was introduced into the same strain (*C. ammoniagenes* ATCC 6872) under control of the IPTG-inducible *tac*-promotor,[28] in addition to its intrinsic gene. This approach required the growth medium to be supplemented with Mn. Nonphysiological levels of all metals, including Mn, were avoided. The typical Mn concentration used to generate Mn-R2F (native-type R2F) was 185 μM $MnCl_2$. The addition of equimolar amounts of Mn^{2+} and Fe^{2+} did not change the level of metalloradical assembly or radical generation in R2F (see below). In addition, if the growth media was only supplemented with Fe^{2+}, no Fe^{2+} was incorporated to a significant extent into R2F and no tyrosyl radical, as measured by its UV/vis absorbance at 408 nm, was observed. Thus, *C. ammoniagenes* restricts the incorporation of Fe into R2F *in vivo* even in the absence of Mn and it is the availability of Mn that is the limiting factor that determines the amount of functional metalloradical cofactor obtained.

The R2F preparation used for the crystal structure and multifrequency EPR measurements detailed below, typically displayed an activity of 69 $\mu mol \cdot mg^{-1} \cdot min^{-1}$. This value exceeds the measured activity of all other RNRs by at least 10-fold, with the exception of *C. glutamicum* (see Supporting Information, Table S1). In addition this value is a thousand-fold higher than that obtained from *C. ammoniagenes* R2F expressed in *E. coli* and reconstituted with Fe (48 $nmol \cdot mg^{-1} \cdot min^{-1}$).[26] In this earlier study the *C. ammoniagenes nrdF* gene was heterologously expressed in *E. coli* and the purified apo-R2F protein was reactivated with Fe^{II}-ascorbate *in vitro*.

The number of Mn per R2F monomer was determined to be 0.74 ± 0.04 by graphite furnace atomic absorption spectroscopy (GF-AAS) and inductively coupled plasma mass spectrometry (ICPMS), see ref 28. By comparison, the number of Fe per monomer was determined to be 0.03 ± 0.04. Thus, the metal cofactor contains at least 1 Mn per R2F monomer and ~0 Fe per R2F monomer. The radical content was estimated to be 0.18 $Y^{\bullet}$ per R2F monomer, from its UV/vis absorption at 408 nm. As the radical content is significantly smaller than 1, only a fraction of centers (20%) contain a fully assembled metalloradical cofactor.

The addition of hydroxyurea (HU), a radical scavenger, to the holoenzyme quenches the tyrosyl radical, inhibiting enzymatic function, see ref 25. Removal of HU, under aerobic conditions, results in the recovery of the holoenzyme's catalytic function.[37] Typically up to 75% of the original activity is observed after removal of the radical scavenger.[37] Quenching of the tyrosyl radical, as measured by its UV/vis absorption at 408 nm, was also observed in this study, upon addition of HU to the purified R2F subunit. Here a tyrosyl radical signal was recovered after HU had been removed via ultrafiltration by the concomitant addition of 10 μM H_2O_2 and 2.5 μM methylviologen (as a mediator). The tyrosyl radical showed rapid and complete recovery within 60 s of H_2O_2 addition. It was noted that the final concentration of the tyrosyl radical signal typically exceeded its initial concentration by 30%. It is unclear whether this additional increase reflects the amount of radical lost during our purification procedure or is derived from newly assembled centers that either contained no Mn cofactor (apo-R2F), or a partially assembled Mn cofactor. Regardless, treatment of the inactivated R2F with H_2O_2 leads to assembly of a functional metalloradical cofactor.

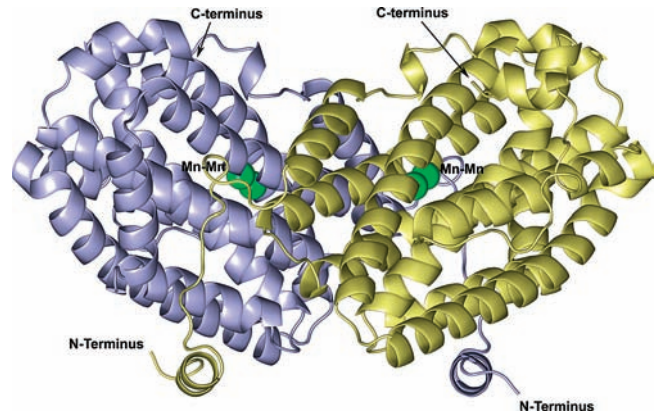

Figure 4. Overall structure of the all helix bundle R2F subunit obtained from *C. ammoniagenes*. The yellow and blue ribbons show the protein backbone of the two monomer units of the dimer. The two Mn atoms in each monomer are shown as green spheres.

A recent report of Cotruvo and Stubbe suggested the involvement of an additional flavodoxin, NrdI in class Ib metallocofactor assembly.[32] In *C. ammoniagenes* the *nrdI* gene is located in the *nrd* operon in front of *nrdE*.[48] In the R2F preparations used for this study we could not identify an equivalent small protein (*C. ammoniagenes*-NrdI acc. no., PDB O69272) as detected by ESI-QTOF mass spectrometry. Attempts to identify this protein in *C. ammoniagenes* form part of ongoing experiments.

4.2. Crystal Structure.

4.2.1. Structure Determination and Overall Structure. Crystals of the R2F subunit of RNR obtained from *C. ammoniagenes* diffracted to 1.36 Å resolution and belonged to the space group *C*2 with unit-cell parameters $a = 96.21$ Å, $b = 87.63$ Å, $c = 83.25$ Å, $\beta = 99.29°$.[42] Figure 4 shows the structure of R2F from *C. ammoniagenes*. The homodimeric protein contains only helical bundles. The overall structure is very similar to the R2F structure reported earlier by Högbom et al.[26] obtained from heterologous expression in *E. coli*.

4.2.2. The Metalloradical Cofactor. X-ray fluorescence spectroscopy (XRF) was carried out in order to determine the metal components of the R2F subunit. Spectra for each metal fluorescence energy range are shown in the Supporting Information (Figure S1). No fluorescence was observed for zinc, copper, cobalt, iron, or nickel (see Figure S1A−C, Supporting Information). However, a manganese signal was observed (see Supporting Information Figure S1D). The results indicate that manganese alone is the native metal of the R2F subunit. The single-wavelength anomalous dispersion (SAD) method was applied to the manganese signal and peak data were collected at an X-ray wavelength of 1.89000 Å (see Table 1). The anomalous difference map revealed four manganese peaks. As the R2F dimer has a noncrystallographic symmetry between the two R2F monomers, the four peaks in the difference map indicate the presence of 2 Mn per R2F monomer. The anomalous difference map for one R2F monomer subunit is shown in Figure

(48) Torrents, E.; Roca, I.; Gibert, I. *Microbiology* **2003**, *149*, 1011–1020.
(49) Almost no electron density was observed at position Oε2 of residue E168. Another set of diffraction data of Mn-R2F solved at 1.65 Å resolution also showed only a weak electron density at this position (data not shown).

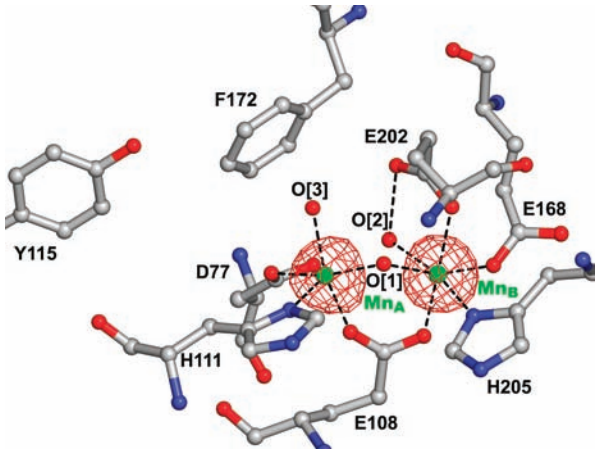

Figure 5. Single-wavelength anomalous dispersion (SAD) of the R2F subunit of *C. ammoniagenes* (monomer). The manganese signal was recoded at 1.89000 Å (see Table 1). The anomalous difference map revealed four manganese peaks, two for each monomer subunit. The difference map (red meshed surface) has been overlaid on the proposed coordination sphere as determined from fitting the electron density map.

5 (red meshed surface). It has been overlaid onto the proposed coordination sphere as determined from the fitting of the electron density map (see Figure 6A). The value of 2 Mn per R2F falls within the allowed range as determined by the chemical analysis (see 4.1). As the metal site uniformly contains two Mn, it is suggested that only the fully assembled R2F protein fraction readily crystallizes. Apo-R2F protein and R2F which contain only 1 Mn center are assumed to crystallize more slowly or not at all.

The electron density map of the metalloradical cofactor of R2F is shown in Figure 6A and the corresponding bond distances in Figure 6B. The metal site contains two Mn centers, Mn_A (proximal to the tyrosine Y115) and Mn_B (distal to the Y115). The Mn−Mn separation is 3.3 Å. Both Mn are coordinated by a histidine residue (H111 for Mn_A and H205 for Mn_B) and bridged by a glutamic acid (E108). Two additional glutamic acids (E202 and E168[49]) coordinate Mn_B; only an aspartate residue (D77) was identified as a coordinating residue to Mn_A. A bridging oxo/hydroxo (O[1]), with Mn−O−Mn bond angle of ∼120° was observed between Mn_A and Mn_B, analogous to the di-iron metallocofactor of class Ia RNRs. A second asymmetric bridging oxygen (O[2]) was also observed. The Mn_A−O[2] bond length (∼2.7 Å) is too long for the O[2] to be considered a real bridging oxo/hydroxo ligand. Instead, it may form part of an extended hydrogen-bonding network about the Mn−Mn core, which possibly includes the aspartate (D77) ligand of Mn_A, 2.7 Å away. A third, terminal hydroxo/water (O[3]) was identified as a ligand to Mn_A. An additional water molecule was not observed between the tyrosine residue Y115 and the hydroxo/water molecule (O[3]) bound to Mn_A. The distance between the center of the tyrosine residue (Y115) and the center of the Mn dimer is approximately 9.8 Å. The hydroxo/water ligation of Mn_A (O[3] in Figure 6B) is 5.6 Å from the tyrosine (Y115) and the edge-to-edge distance of the Mn_A to Y155 is 6.8 Å. It is also noted that the tyrosyl radical has probably significantly decayed during the crystallization process.

The Mn metalloradical cofactor (Mn-R2F) described here is significantly different from earlier inactive structures described in the literature. Both Högbom et al.[26] (PDB ID 1kgp) and Atta et al.[50] have reported crystal structures of the Mn-R2F/Mn-R2 subunit that contained a $Mn^{II}Mn^{II}$ dimer (Figure 6C). Both structures were obtained from apo-R2F/R2 protein that was subsequently reloaded with Mn^{II} *in vitro*. These structures more closely resembled the reduced protein obtained for the diferrous metallocofactor (Fe-R2F) as described below, which was assigned to a resting form of the enzyme.

The diferric metalloradical cofactor (Fe-R2F), previously reported by Högbom et al., was obtained from heterologous expression in *E. coli* and reactivation of the protein by treatment with Fe^{II}-ascorbate *in vitro*.[26] The crystal structure of the Fe-R2F subunit obtained using this preparatory approach showed that two iron centers had been incorporated into the metal binding site and UV/vis measurements confirmed that the R2F subunit contained a tyrosyl radical (0.26 per R2F protein subunit). The Fe-R2F was shown to exist in two stable forms. In its reduced form (PDB ID 1kgo), prior to its activation with O_2, the metal cluster contained two ferrous centers that are separated by ∼4 Å and bridged by two glutamic acids. In its active oxidized form (PDB ID 1kgn), the met state, the cluster contained two ferric centers with a center-to-center separation of ∼3.5 Å and, in addition to a carboxylate bridge, an oxo bridge derived from O_2 (Figure 6D). Figure 7 compares the structures of the metalloradical cofactor of R2F containing either a dimanganese or di-iron R2F (met state) from *C. ammoniagenes*. The overall architecture of the Fe containing dimeric unit is highly similar to the Mn metalloradical cofactor seen in the present work. Only small changes between the two structures are observed: (i) the ring plane of the Phe172 is rotated in the Mn-R2F, displacing a water molecule that is present in the corresponding Fe-R2F and; (ii) the carboxylate of Asp77 has changed its orientation relative to the Mn site, with both oxygens now providing a ligand and/or hydrogen bond to the metallocofactor (see above). The absence of a water molecule between Y115 and the Mn dimer in the Mn-R2F (in addition to O[3]) indicates that the hydrogen bonding networks about the Y115 are different in the Mn-R2F and Fe-R2F proteins.

4.3. Multifrequency EPR Measurements.

4.3.1. Frozen Solution CW X-Band Measurements at 80 K: Detection of a Tyrosyl Radical. A radical signal (at g ∼ 2.004) was observed at $T = 80$ K in Mn-R2F sourced from *C. ammoniagenes* that is similar to a tyrosyl radical (Figure 8, trace A). The signal's hyperfine structure is typical of tyrosyl radical signals observed in RNR class Ib as shown in Figure 8, trace C. Trace C represents a simulated spectrum of a tyrosyl radical using the hyperfine parameters observed for *Salmonella typhimurium*.[51] The simulation can, however, not explain the broadened line shape of the signal. The overall signal profile matches a Lorentzian line shape as shown in Figure 8, trace B. It was also observed that the maximum available microwave power of 200 mW did not saturate the radical at 80 K. These two observations suggest that the tyrosyl radical is not isolated but instead interacts with another paramagnetic species.

4.3.2. Frozen Solution CW X-Band Measurements at 5−30 K: Manifestation of a 'Split-Tyrosyl Radical' Signal. At cryogenic temperatures (<30 K) the appearance of the X-band EPR signal of the tyrosyl radical changes dramatically. A broader signal was observed with spectral features that extend over a field range of ∼40 mT (Figure 9, black traces). The total

(50) Atta, M.; Nordlund, P.; Aberg, A.; Eklund, H.; Fontecave, M. *J. Biol. Chem.* **1992**, *267*, 20682–20688.

(51) Allard, P.; Barra, A. L.; Andersson, K. K.; Schmidt, P. P.; Atta, M.; Gräslund, A. *J. Am. Chem. Soc.* **1996**, *118*, 895–896.

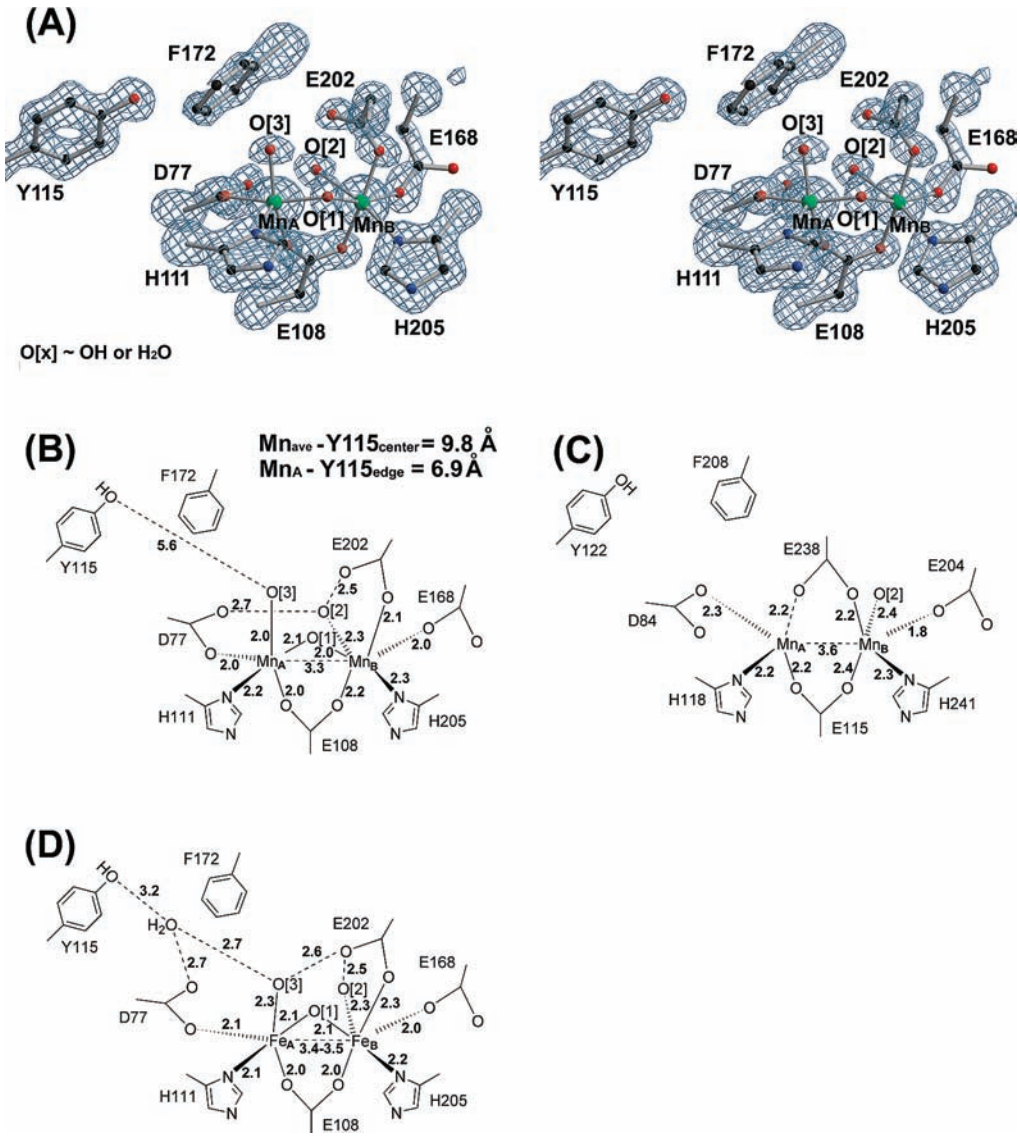

Figure 6. (A) Stereoview of the electron density map of the metalloradical cofactor with surrounding amino acid residues of the R2F subunit obtained from *C. ammoniagenes*. (B) The structure and the coordination distance (Å) of the native-type Mn-R2F from *C. ammoniagenes*. (C) The Mn-substituted form of the R2 protein obtained from *E. coli*.[50] (D) Fe-R2F subunit (in the oxidized form) of *C. ammoniagenes*.[26]

spectral breadth of the signal is significantly larger than that expected for an isolated tyrosyl radical. In addition, the new signal is highly structured at <20 K; at least five features were observed, centered at $g \approx 2.00$ (Figure 9A−C). The temperature dependence of all signals within the 310−370 mT magnetic field range obeys Curie's law (between 5 and 80 K). This suggests that both the signals at low (5 K) and high (80 K) temperatures arise from the same spin manifold. Similar broadened split-tyrosyl radical signals were recently observed at X-band for the metalloradical cofactor of R2F sourced from *E. coli* (class Ib), reactivated *in vitro* with Mn.[32] However, no theoretical rationale for the metalloradical cofactor signal was presented.

4.3.3. Frozen Solution CW Q-Band Measurements at 10−40 K: An Analogous 'Split-Tyrosyl Radical' Signal As Seen at X-Band. A 'split-tyrosyl radical' was also seen at cryogenic temperatures (<40 K) at Q-band. It displays the same basic characteristics as seen at X-band, namely: (i) it is centered about g∼2; its total spectral breadth is approximately 40 mT; and it resolves a peak splitting of 4−6 mT. The temperature dependence at Q-band was also nominally the same. The wings of the signal were most readily resolved at 10 K, with their intensity decreasing relative to the central line as the temperature increased. The Q-band spectrum resolves more peak splittings than seen at X-band. These new features are unlikely to be due to an enhanced Zeeman effect as no net change in the total spectral breadth is observed. The additional splitting seen at Q-band, which manifests itself at X-band in an asymmetric line shape of several peaks (see peaks 1 and 4, Figure 9A), is a further indication of the complex spin manifold the tyrosyl radical species is interacting with.

4.3.4. Powder Pattern CW X/Q-Band Simulations: A $Mn^{III}Mn^{III}Y^{\bullet}$ or $Mn^{IV}Mn^{IV}Y^{\bullet}$ Metalloradical Cofactor. The spectral widths of the EPR signals seen at 9 and 34 GHz are consistent with the tyrosyl radical weakly interacting with the two Mn centers. These spectra can be considered, to zeroth order, as an isolated tyrosyl radical that is perturbed by its interaction with a nearby paramagnetic center. This interaction is of the order of the radical's intrinsic line width (∼100 MHz/3.6 mT). The split-tyrosyl radical signal of the R2F subunit of *C. ammoniagenes* splits into 5 discrete lines at X-band, with an unperturbed central line, suggesting the tyrosyl radical must

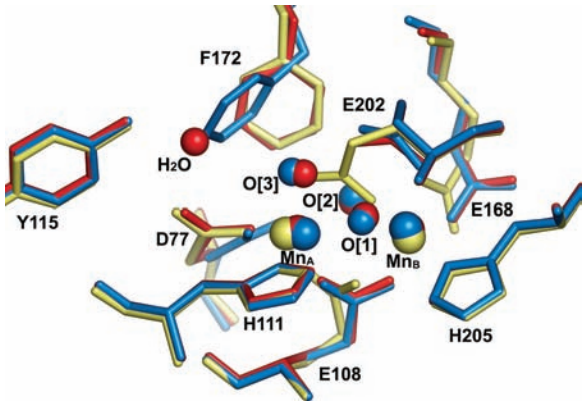

Figure 7. Comparison of the metalloradical cofactor of R2F that contains: an oxidized (active) Mn_2 cofactor (blue), a reduced (inactive) Mn_2 cofactor (yellow) or an oxidized (active) Fe_2 cofactor (red). The Mn-R2F (reduced) and Fe-R2F (oxidized) structures are taken from Högbom et al.[26] (PDB ID 1kpg, 1kgn). The ring plane of the F172 is rotated in the Mn-R2F (oxidized), displacing a water molecule as compared to the corresponding Fe-R2F. The carboxylates E202 and D77 change their orientation relative to the Mn site in the reduced and oxidized structure. E202 provides one ligand to the metallocofactor in its oxidized state (blue). In its reduced state, E202 is a bidentate ligand, bridging the two Mn (yellow). Similarly, both oxygens of D77 provide a ligand and/or hydrogen bond to the metallocofactor in its oxidized state. In its reduced state it provides only one ligand (yellow), similar to the Fe_2 cofactor (red).

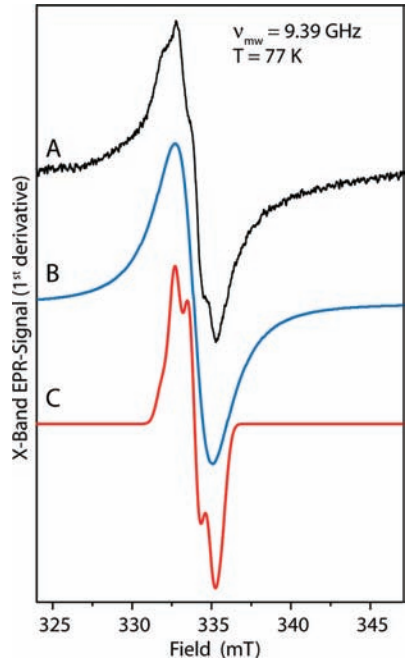

Figure 8. CW X-band EPR of the R2F subunit of *C. ammoniagenes*. (A) X-band spectrum recorded at 77 K; (B) a fitted Lorentz line shape (first derivative). A Lorentz line well reproduces the overall line shape suggesting a dominantly homogeneous line-broadening mechanism; and (C) a simulation assuming parameters typical for a class Ib RNR tyrosyl radical, (see Supporting Information Table S2). Experimental conditions: microwave frequency 9.39 GHz, microwave power 2 mW, $T = 77$ K, modulation amplitude 0.16 mT, modulation frequency 100 kHz, 9 scans of 84 s, time constant 82 ms.

interact with a metal center of integer spin ($S \geq 2$). A total spin of 2 ($S = 2$) corresponds to a $Mn^{V}Mn^{V}$ dimer, which is considered to be not physically realizable. The only oxidation states of the two Mn centers that are considered plausible are: Mn^{II}, Mn^{III} and Mn^{IV}. This allows for five possible Mn oxidation state configurations. It can immediately be deduced that a tyrosyl

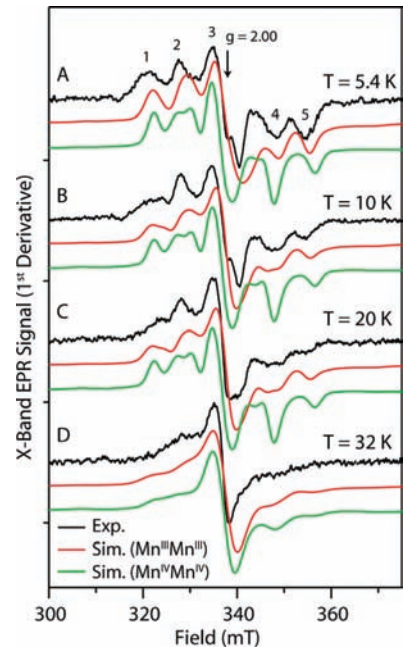

Figure 9. The temperature dependence of the CW X-band EPR spectrum of the R2F-subunit of *C. ammoniagenes* in frozen solution. Black lines: experimental data; red lines: simulations assuming the R2F subunit contain a $Mn^{III}Mn^{III}$ dimer; green lines: simulations assuming a $Mn^{IV}Mn^{IV}$ dimer. Simulation parameters are given in Table 2. Experimental conditions for A, B, C, and D: microwave frequency 9.47 GHz, microwave power 2 mW, field modulation 1.2 mT, modulation frequency 100 kHz, accumulation time 84 s, time constant 164 ms.

Table 2. Optimized Simulation Parameters Used for Simulations at 9, 34, and 244 GHz Shown in the Text for the $Mn^{III}Mn^{III}$ Dimer and $Mn^{IV}Mn^{IV}$ Dimer Simulations (see Figures 9, 10 and 11)

		fit value in MHz (cm^{-1})					
		$Mn^{III}Mn^{III}$			$Mn^{IV}Mn^{IV}$		
J		17688 (0.59)			80644 (3.48)		
Mn_A	D_A	24714 (0.82)			24809 (0.83)		
	E_A/D_A	0.10			0.10		
Mn_B	D_B	27582 (0.92)			27308 (0.91)		
	E_B/D_B	0.25			0.27		
g_{Mn}		2.026			2.025		
J_{int}		ISO	−28.9		ISO	−19.3	
		X	181.6	210.5[a]	X	219.4	238.7[a]
		Y	−130.0	−101.1[a]	Y	−183.0	−163.7[a]
		Z	−138.4	−109.5[a]	Z	−94.2	−74.9[a]
G_{tyr} (Collinear)		ISO	2.0050		ISO	2.0048	
		X	2.0046	−0.0004[a]	X	2.0052	0.0004[a]
		Y	2.0077	0.0027[a]	Y	2.0032	−0.0016[a]
		Z	2.0028	−0.0022[a]	Z	2.0060	0.0012[a]
g_{tyr} (Rotated)		iso	2.0051		iso	−[c]	
		x	2.0085	0.0034[a]	x	−	−
		y	2.0045[b]	−0.0006[a]	y	−	−
		z	2.0022[b]	−0.0029[a]	z	−	−
		α	67.2		−		
		β	30.0		−		

[a] Anisotropic component, i.e. $g_X' = g_X - g_{ISO}$; $J_X' = J_X - J_{ISO}$. [b] Fixed simulation parameters, i.e. g_y and g_z. [c] $Mn^{IV}Mn^{IV}$ simulation was unable to reproduce the experimental spectrum at high field using fitting procedure (ii), i.e. $g_y = 2.0045$, $g_z = 2.0022$.

radical coupled to the mixed valence complexes $Mn^{III}Mn^{II}$ and $Mn^{III}Mn^{IV}$ would not be able to reproduce the split pattern observed. Their spin manifolds contain only paramagnetic sublevels. As a consequence, a fitted exchange interaction between the Mn cluster and the tyrosyl radical cannot simultaneously explain both the unperturbed central line ($g \approx 2.00$) and the total width of the split signal.[52] Only the equivalent

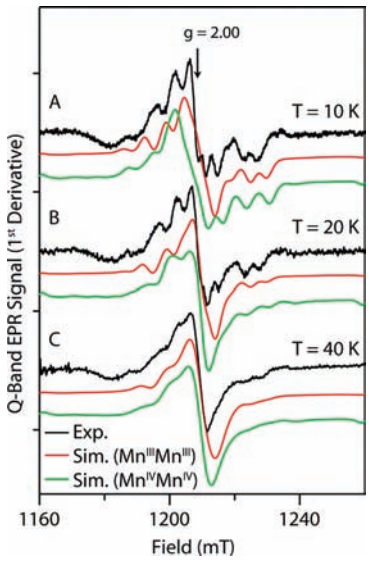

Figure 10. Temperature dependence of the CW Q-band EPR spectrum of the R2F-subunit of *C. ammoniagenes* in frozen solution. Black lines: experimental data; red lines: simulations assuming the R2F subunit contains a $Mn^{III}Mn^{III}$ dimer; green lines: simulations assuming a $Mn^{IV}Mn^{IV}$ dimer. Simulation parameters are given in Table 2. The negative feature at 1170 mT represents a baseline artifact. Experimental conditions for A, B, and C: Microwave frequency 33.94 GHz, field modulation 1.0 mT, 100kHz, 10 scans; accumulation time 84 s; time constant 82 ms.

oxidation state configurations: $Mn^{II}Mn^{II}$, $Mn^{III}Mn^{III}$ and $Mn^{IV}Mn^{IV}$ are considered feasible. It is also noted that the $Mn^{II}Mn^{II}$ oxidation state is inconsistent with crystallographic data (see Results 4.2 above) and mechanistic constraints (see Discussion). Thus, only simulations for the $Mn^{III}Mn^{III}$ and $Mn^{IV}Mn^{IV}$ configurations are presented.

Powder simulations of the 'split-tyrosyl radical' signal at X- and Q-bands are shown in Figures 9 and 10, (red trace assuming a $Mn^{III}Mn^{III}$ dimer, green trace assuming a $Mn^{IV}Mn^{IV}$ dimer). A simple rationale can be made for the 'split-tyrosyl radical' as given in the Theory section (see Figure 2). The low- and high-field edges of the split signal are derived from the tyrosyl radical's interaction with the Mn−Mn spin multiplet of highest effective spin, $S_T = 4$ for a $Mn^{III}Mn^{III}$ dimer.[53] As these features are most readily observed at low temperatures, the Mn−Mn manifold state of highest spin multiplicity must be the ground state. As a consequence the coupling between the two Mn centers must be ferromagnetic. Transitions within higher effective multiplets ($S = 3$, 2, 1, and 0) are progressively narrower (see ref 47, Theory), and add intensity to the center of the pattern (i.e., at $g \approx 2.0$). At 5 K, transitions within the ground multiplet dominate the powder spectrum. As the temperature is raised to 30 K, the relative population of higher multiplet states increases and thus the total signal at either X- or Q-bands appears to narrow; the relative intensity of the wings of the split signal decrease compared to the unperturbed central line. The superposition of the different multiplet states leads to the additional splittings seen at both X and especially Q-band. The strong temperature dependence of the 'split-tyrosyl radical' signal suggests that the energy level separations between the Mn−Mn multiplet states are small. The spin manifold ladder spacing is dominantly dependent on *J*, the coupling between the two Mn centers (see Figure 3).

The $Mn^{III}Mn^{III}$ model reproduces both the line shape and temperature dependence of the 'split-tyrosyl radical' signal significantly better than the $Mn^{IV}Mn^{IV}$ model at both X and Q-band frequencies. The $Mn^{IV}Mn^{IV}$ model predicts peak splittings not observed in the experimental data and the simulated line shape is approximately invariant over the 5−20 K temperature range. This disparity between the $Mn^{IV}Mn^{IV}$ model and the experimental data arises from the simulations' inability to fit the isotropic exchange J between the two Mn in the two temperature regimes. To reproduce the 'five-peak pattern' seen at 5 K at X-band (Figure 9A), *J* has to be of the order of several cm^{-1}. In contrast, to fit the temperature dependence (5−30 K) the exchange interaction must be small, less than 1 cm^{-1}. The fitted value of ∼3.5 cm^{-1} represents a compromise between these two competing constraints. This problem is not encountered for the $Mn^{III}Mn^{III}$ simulation. It estimates the *J* coupling between the two Mn to be ∼0.7 cm^{-1}. The small Mn−Mn exchange then readily accounts for the temperature dependence of the 'split-tyrosyl radical' signal.

The invariance of the 'split-tyrosyl radical' signal's width at X- and Q-bands frequencies is consistent with the notion that the nonfield dependent terms of the spin Hamiltonian i.e. $\mathbf{J}_{int}$, dominantly defines the total spectral breadth of the signal. The fitted exchange tensor ($\mathbf{J}_{int}$), for the $Mn^{III}Mn^{III}$ simulation, is axially symmetric and is virtually traceless suggesting the interaction between the tyrosyl radical and the two Mn centers is dominantly dipolar (i.e., $\mathbf{J}_{int} \approx \mathbf{d}_{dip}$, see Theory). The magnitudes of the tensor components are also consistent with this interpretation. The largest component of the $\mathbf{d}_{dip}$ tensor d_{dipX} (∼200 MHz), assigns the inter-Mn−Tyrosyl vector (Table 2) and corresponds to an average interspin distance (*r*) between the tyrosyl radical and each Mn center of ∼8 Å, approximately that seen in the crystal structure (see Results 4.2).

4.3.5. Frozen Solution High-Field (244 GHz) CW EPR Measurements. Cryogenic (5 K) CW EPR experiments of the tyrosyl radical of the R2F subunit were also carried out at high field (244 GHz). A 'radical-like' signal was observed with *effective* **g**-tensor components of 1.9989, 2.0040, and 2.0105 (see Figure 11, black trace). These values are unusual for a protein based radical; the intrinsic **g**-tensor values for the stable tyrosyl radical of the R2F subunit of *S. typhimurium* are 2.0022, 2.0045, and 2.0089.[51] Thus the observed tyrosyl radical seen here is approximately 3 times the spectral breadth of the tyrosyl radical observed in *S. typhimurium*. An estimate of the expected total spectral breadth of the high-field signal can be made from the low frequency X- and Q-band data. At these frequencies the total breadth of each signal was ∼40 mT. It can be shown by simulation that the spectral breadth of the split-tyrosyl radical signal at these frequencies is dominantly dependent on the Mn−tyrosyl exchange interaction (see above, and Theory). At high field (244 GHz) this is no longer the case. The total breadth now includes the broadening due to the exchange interaction and the intrinsic g-anisotropy of the tyrosyl itself. An estimate of the latter contribution can be made from literature data of isolated tyrosyl radical signals, by taking the difference between the g_X and g_Z values, the edges of the tyrosyl radical spectrum, in magnetic field units i.e. $(1/g_Z - 1/g_X)\cdot\nu\cdot h/\beta$ where h, β and ν are Planck's constant, the Bohr magneton, and the microwave

(52) The exchange interaction (J_{int}) has to be both smaller than the linewidth of the unperturbed tyrosine radical to resolve the central ($g \approx 2.00$) component of the signal and significantly larger than the linewidth of the tyrosyl to resolve the total width of the split signal.

(53) A description of the Mn dimer's energy levels in terms of the 'effective spin' S_T of the different sub-manifolds of the metal is used for convenience. This description is not valid for the $Mn^{III}Mn^{III}/Mn^{IV}Mn^{IV}$ models presented here since the 'ground' spin multiplet is not well removed from the higher effective spin states.

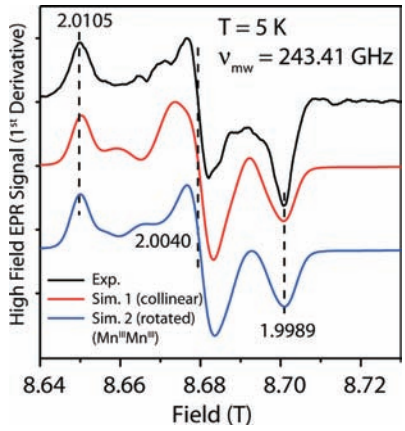

Figure 11. CW high-field EPR spectrum of the R2F-subunit of *C. ammoniagenes* in frozen solution. Black line: experiment; red line: simulation assuming the molecular **g**-tensor of the tyrosyl radical is collinear with the principal axis system of the spin Hamiltonian model (i.e., Mn_A and Mn_B, parameter set given in Table 2); blue line: simulation assuming typical tyrosyl radical **g**-tensor components and an axes rotation of the tyrosyl radical relative to the principal axis system of the spin Hamiltonian model (see Table 2). Additional simulations, where the fitted line width was varied, are shown in the Supporting Information. The data was collected using passage conditions. The absorption-like line shape obtained was pseudomodulated (2 mT amplitude) to obtain the derivative mode line shape presented. Experimental conditions: microwave frequency 243.41 GHz; microwave power: 5 mW; temperature 5 K.

frequency, respectively. At 244 GHz this relation yields an intrinsic tyrosyl radical width of ∼20 mT, assuming $g_X = 2.0080$ and $g_Z = 2.0022$. The sum of the Mn−tyrosyl exchange and the *g*-anisotropy of the tyrosyl radical gives a total spectral breadth of ∼60 mT, the same as seen experimentally (see Figure 11).

As the high-field (244 GHz) spectrum now contains contributions from the intrinsic *g*-anisotropy, a substantial increase in the number of spectral peaks that make up the composite line shape is expected. This is not observed; the experimental spectrum contains fewer peaks than that obtained at X-band. This effect arises from *g*-strain, a distribution in spin Hamiltonian parameters, that is enhanced at high magnetic fields. This is discussed further in the Supporting Information.

4.3.6. CW High-Field Powder EPR Simulations: Orientation of the Tyrosyl Relative to the $Mn^{III}Mn^{III}$ Dimer. The high-field spectrum can be simulated using the same spin Hamiltonian model as used for the X- and Q-band spectra, see above and the Theory section (Table 2). The parameter set employed to simulate the high-field spectrum was fixed such that the exchange and zero-field splitting parameters as determined for the X- and Q-band simulations were kept constant. Two fitting procedures were then employed: (i) the molecular frame of the tyrosyl radical was assumed to be collinear with the axis system of the spin Hamiltonian model. The high-field spectrum was then fitted by varying the **g**-tensor components of the tyrosyl radical (G_X, G_Y, G_Z); and (ii) the molecular **g**-tensor components (g_x, g_y, g_z) along g_y and g_z were fixed to values typically seen for tyrosyl radicals i.e. $g_y = 2.0045$, $g_z = 2.0022$ (see Supporting Information Table S2). The high-field spectrum was then fitted by varying the value of g_x and the orientation of the molecular frame relative to the axis system of the spin Hamiltonian model (α,β). As the spin Hamiltonian model assigns only one principal axis (*X*), which is aligned along the Mn−Tyr interspin vector, only two rotations are required to map the molecular frame to the model's axis system. The third Euler rotation is undefined in the model presented. Both of the two fitting procedures ((i) and (ii)) have the same number of free variables, i.e. 3.

The simulation ($Mn^{III}Mn^{III}$) assuming a collinear molecular frame for the tyrosyl radical (procedure (i)) is shown in Figure 11 (red trace). The obtained **g**-tensor components [G_X, G_Y, G_Z] for the $S = {}^1/_2$ radical are: $G_X = 2.0046$, $G_Y = 2.0077$, and $G_Z = 2.0028$, which are similar to those seen for tyrosyl radicals. (see Supporting Information Table S2, reproduced from[54]). The largest deviation is seen for the G_Z component. The g_z principal component, in the molecular frame of a tyrosyl radical, is along the p_z (π) orbitals of the aromatic ring of the tyrosyl radical,[55−58] perpendicular to the ring plane. It magnitude is approximately that of the free electron (2.0023). The observed difference between this value and the measured one demonstrates that the molecular **g**-tensor of the tyrosyl radical and the coordinate system of the model are not exactly collinear. A similar simulation assuming a $Mn^{IV}Mn^{IV}$ dimer gives an axial **g**-tensor [G_X, G_Y, G_Z] of $G_X = 2.0052$, $G_Y = 2.0032$, and $G_Z = 2.0060$, significantly different from that typically seen for a tyrosyl radical (not shown).

The simulation ($Mn^{III}Mn^{III}$) assuming typical tyrosyl **g**-tensor components (procedure (ii)) is shown in Figure 11 (blue trace). The obtained g_x was 2.0085 and the α and β rotations were 67° and 30°, respectively. The g_x component typically has values of 2.006−2.009 (see Supporting Information Table S2, reproduced from[54]). Unlike g_y and g_z, g_x is highly sensitive to the hydrogen bonding environment of the tyrosyl radical. A large g_x value indicates the phenolic oxygen is deprotonated.[55−58] Thus, the simulation suggests that the tyrosyl radical of *C. ammoniagenes* is deprotonated and probably only weakly hydrogen bonded.[55−58] A similar simulation, assuming a $Mn^{IV}Mn^{IV}$ dimer and typical tyrosyl g-tensor components (procedure (ii)), can not reproduce the three main turning points seen in the high-field spectrum (not shown).

As stated in the Theory and Results sections above, one of the principal axes of the spin Hamiltonian model can be deduced from the traceless (dipolar, $\mathbf{d}_{dip}$) component of the coupling tensor $\mathbf{J}_{int}$. As the largest tensor component of $\mathbf{d}_{dip}$ is d_{dipX} the X-/Q-band simulations assign the inter-Mn−tyrosyl vector along the *X*-axis of the spin-system model. The molecular g-tensor axes for a tyrosyl radical are aligned such that, g_x is along the C−O bond, g_y bisects the ring plane, perpendicular to the C−O bond and g_z is perpendicular to the ring plane. The relative orientation of the molecular axis of the tyrosyl radical (*x*,*y*,*z*) to the coordinate system used for the spin Hamiltonian model (*X*,*Y*,*Z*), as determined by fitting procedure (ii) is shown in Figure 12A in the g_x/g_y and g_x/g_z planes. The α angle corresponds to a rotation about the molecular g_z axis, i.e. it corresponds to a rotation of the tyrosyl ring plane. The β angle corresponds to a rotation about the molecular g_y axis, i.e. it corresponds to a rotation out of the ring plane of the tyrosyl.

The molecular **g**-tensor arrangement as described above compares favorably with the crystal structure. A mapping of

(54) Schünemann, V.; Lendzian, F.; Jung, C.; Contzen, J.; Barra, A.-L.; Sligar, S. G.; Trautwein, A. X. *J. Biol. Chem.* **2004**, *279*, 10919–10930.
(55) Gerfen, G. J.; Bellew, B. F.; Un, S.; Bollinger, J. M.; Stubbe, J.; Griffin, R. G.; Singel, D. J. *J. Am. Chem. Soc.* **1993**, *115*, 6420–6421.
(56) Un, S.; Gerez, C.; Elleingand, E.; Fontecave, M. *J. Am. Chem. Soc.* **2001**, *123*, 3048–3054.
(57) Faller, P.; Goussias, C.; Rutherford, A. W.; Un, S. *Proc. Natl. Acad. Sci. U.S.A.* **2003**, *100*, 8732–8735.
(58) Biglino, D.; Schmidt, P. P.; Reijerse, E. J.; Lubitz, W. *Phys. Chem. Chem. Phys.* **2006**, *8*, 58–62.

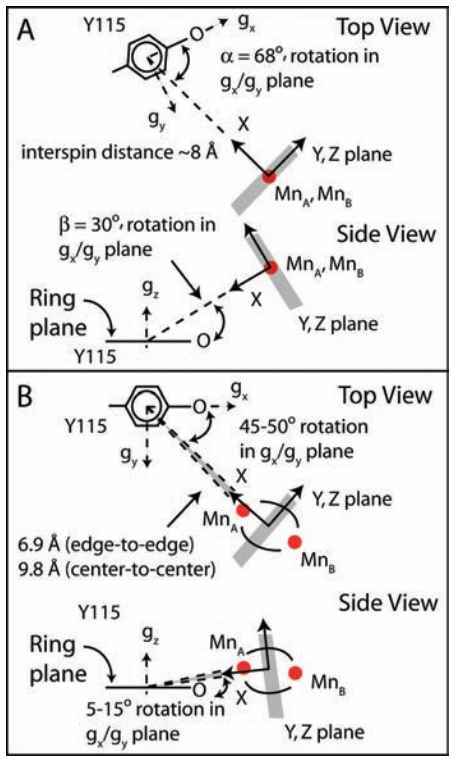

Figure 12. (Panel A) The orientation of the tyrosyl radical (Y115) relative to the Mn dimer, as determined by the multifrequency EPR simulation (assuming a $Mn^{III}Mn^{III}$ dimer). (Panel B) The orientation of the tyrosyl radical (Y115) relative to the Mn dimer as seen in the crystal structure. The coordinate system (*X*,*Y*,*Z*) of the simulation is marked along with the intrinsic g-tensor of the tyrosyl radical (*x*,*y*,*z*). The *X* direction is along the interspin vector connecting the Mn dimer to the tyrosyl radical, the *Y*, *Z* directions are not explicitly assigned, they define a plane perpendicular to *X*.

the (*X*,*Y*,*Z*) coordinate system of the spin Hamiltonian model, onto the molecular (*x*,*y*,*z*) coordinate system of the tyrosyl radical using the crystal structure is shown in Figure 12B in the g_x/g_y and g_x/g_z planes. As expected from the EPR simulations, the principal axis system of the tyrosyl radical **g**-tensor (*x*, *y*, *z*), which is assumed to be collinear with the molecular axes of Y115, is not collinear with the axis system (*X*, *Y*, *Z*) of our spin Hamiltonian model. The crystal structure predicts the ring plane of the tyrosine is rotated 45−50° and is tilted 5−15° out of the plane (about the g_y axis). The variation in the angles reported comes from the degree of uncertainty in assigning the interspin vector. The two limits given refer to the interspin vector assigned such that it connects the center of the tyrosyl ring with Mn_A or the center of the tyrosyl to the midpoint of the Mn−Mn separation. These two rotations are similar to those predicted by the EPR simulation; each differs by ~20°. It is not clear at present whether this discrepancy is reporting a real structural difference between the crystallized metalloradical cofactor and the solution sample used for EPR or arises from the many simplifications used to model the system, i.e. collinear axes of the two Mn ions, an average Mn−tyrosine exchange tensor, etc. It is noted that during the crystallization procedure, the tyrosyl radical almost completely decays. Thus, the difference in the orientation of the tyrosyl radical may report on a change in the hydrogen-bonding network upon formation of the tyrosyl radical. This would suggest that tyrosyl radical generation is coupled to proton movement. This phenomenon has been observed for other redox active tyrosines, e.g. tyrosine *Z* of the D1 protein of PS II.[57] Further experiments are planned on single crystals of the R2F subunit to resolve this question.

5. Discussion

The experimental results and theoretical modeling shown above demonstrate that the dominant *in vivo* form of the native metalloradical cofactor of the R2F subunit of *C. ammoniagenes* RNR contains only Mn. This is in contrast to a newly discovered class of RNR, isolated from *Chlamydia trachomatis*, which contains a Mn−Fe metallocofactor and harbors phenylalanine in the place of tyrosine[7−10] i.e. it lacks a tyrosyl radical. The metalloradical cofactor of *C. ammoniagenes* instead contains a μ-oxo-Mn−Mn complex, analogous to the diferric metallocofactor seen in the R2 subunit of class Ia RNRs. The oxidation state of the metal site and possible mechanism of radical generation of this new, active Mn-R2F subunit is discussed below.

5.1. Comparison to Split Radical Signals Found in the Literature. The metalloradical cofactor of R2F displays a coupled radical signal or 'split signal'. These types of signals have previously been observed in other biological systems with redox active tyrosine residues, in particular in PS II.[59−62] Here the isolated tyrosyl radical, typically of width ~3 mT (full width half-maximum), is broadened by its weak interaction with a paramagnetic center, the oxygen evolving complex (OEC), a tetra-manganese cofactor located approximately ~7 Å away. In a similar fashion, the tyrosyl radical of the R2F subunit, is broaden by its interaction with a Mn−Mn dimer that is approximately ~8 Å away from the radical, (see Results 4.2 above). It is also noted that the 'split-tyrosyl radical' signal seen in PS II collapses at temperatures above ~90 K, i.e. the resolved 'splitting' (<10 mT peak-to-peak separation) seen at 5 K is lost upon warming to 90 K, where an unperturbed tyrosyl radical signal is then resolved.[63,64] This is nominally the same phenomenon as that observed for Mn-R2F (see Figure 8) and is the result of exchange narrowing.[46,65,66] At higher temperatures, the distinct 'split-tyrosyl radical' transitions of the spin manifold, which correspond to each line of the split signal pattern, interchange at frequencies exceeding the energy-level separation. Under these conditions a single average transition is observed, whose exact line shape depends upon the interchange frequencies within the spin manifold. The line shape of such signals appears as a broadened Lorentzian line.[66] The same line shape is observed at 77 K for the tyrosyl in Mn-R2F confirming that this signal is indeed an exchange narrowed species (Figure 8, traces A and B).

A similar coupled radical signal is observed for the metalloradical cofactor of the R2F subunit of *C. glutamicum*.[29]

(59) Koulougliotis, D.; Teutloff, C.; Sanakis, Y.; Lubitz, W.; Petrouleas, V. *Phys. Chem. Chem. Phys.* **2004**, *6*, 4859–4863.
(60) Havelius, K. G. V.; Su, J.-H.; Feyziyev, Y.; Mamedov, F.; Styring, S. *Biochemistry* **2006**, *45*, 9279–9290.
(61) Su, J. H.; Havelius, K. G. V.; Ho, F. M.; Han, G.; Mamedov, F.; Styring, S. *Biochemistry* **2007**, *46*, 10703–10712.
(62) Cox, N.; Ho, F. M.; Pewnim, N.; Steffen, R.; Smith, P. J.; Havelius, K. G. V.; Hughes, J. L.; Debono, L.; Styring, S.; Krausz, E.; Pace, R. J. *Biochim. Biophys. Acta* **2009**, *1787*, 882–889.
(63) Ioannidis, N.; Zahariou, G.; Petrouleas, V. *Biochemistry* **2008**, *47*, 6292–6300.
(64) Zahariou, G.; Ioannidis, N.; Sioros, G.; Petrouleas, V. *Biochemistry* **2007**, *46*, 14335–14341.
(65) Abragram, A.; Bleaney, B. *Electron Paramagnetic Resonance of Transition Metal Ions*; Clarendon Press: Oxford, 1970.
(66) Pake, G. E.; Estle, T. L. *The Physical Principles of Electron Paramagnetic Resonance*, 2nd ed.; Benjamin: Reading, MA, 1973.

However, the split-tyrosyl radical signal seen at X-band for this species is approximately half the spectral width seen in this study. This result is unusual considering the substantial sequence homology of the nrdF gene sourced from the two species. While we have not attempted a robust fitting of these spectra, we are confident that the spectra of *C. glutamicum* can be simulated using an identical spin Hamiltonian model presented in this work. The key difference between the two species could be the sign of the exchange interaction between the two Mn^{III} centers. For *C. ammoniagenes* the coupling between the two Mn centers is weakly ferromagnetic whereas the coupling between the two Mn centers of *C. glutamicum* is suspected to be weakly antiferromagnetic. This would redistribute the signal intensities of individual peaks in the split pattern. As the ground state for *C. glutamicum* is $S = 0$, the central line(s) of the split pattern ($g \approx 2$) appears more intense at low temperatures as compared to the wings of the split signal. Thus the split tyrosyl radical signal seen in *C. glutamicum* at low temperature (10 K)[29] should resemble the higher temperature spectra (≥30 K) seen for *C. ammoniagenes* (Figure 9). It is noted that that the exchange coupling observed for metal dimer complexes, with virtually the same ligand sphere, is usually the same. However, a characteristic feature of the model $Mn^{III}Mn^{III}$ complexes of the type that match the structure of the metallocofactor of R2F (see next section) is the large variation in the Mn−Mn coupling between the two Mn centers. The magnetic coupling between the two Mn centers ranges from strongly antiferromagnetic (-100 cm^{-1}) to weakly ferromagnetic (10 cm^{-1}). Thus small perturbations in the ligand environment of the metallocofactor could dramatically change the Mn−Mn coupling and as a consequence, the observed split tyrosyl radical signal.

5.2. Oxidation State of the Metalloradical Cofactor: A $Mn^{III}Mn^{III}$ Dimer. The oxidation states of the two Mn centers can be deduced from a concomitant analysis of our EPR and crystallographic results. In particular, the structure of the 'split-tyrosyl radical' signal observed at X- and Q-band frequencies, reports on the energy levels of the Mn−Mn dimer system and thus the oxidation state of the two metal centers. The only oxidation states of the two Mn centers that are considered plausible are: Mn^{II}, Mn^{III} and Mn^{IV}. This allows for 5 possible Mn oxidation state configurations. Of these only the $Mn^{III}Mn^{III}$ oxidation state configuration is consistent with all crystallographic and EPR data. The arguments leading to this conclusion are as follows:

(i) The crystallographic data disfavor the $Mn^{II}Mn^{II}$ configuration. Earlier inactive structures in both *C. ammoniagenes* and *E. coli*,[26,50] which contained a $Mn^{II}Mn^{II}$ dimer, are structurally dissimilar to the metalloradical cofactor structure seen here. The active form contains an oxo/hydroxo-bridged Mn motif that is absent in the reduced ($Mn^{II}Mn^{II}$) structures. In addition, the bridging ligands between the two Mn centers resemble structural motifs of model complexes that contain at least one Mn center with oxidation number higher than two. The $Mn^{II}Mn^{II}$ oxidation state also does not provide a mechanism for radical formation.

(ii) The mixed valence $Mn^{II}Mn^{III}$ and $Mn^{III}Mn^{IV}$ configurations cannot readily explain the structure of the 'split tyrosyl radical' signal at X- or Q-band. Their spin manifolds only contain paramagnetic sublevels. As a consequence, a fitted exchange interaction between the Mn cluster and the tyrosyl radical cannot simultaneously explain both the unperturbed central line ($g \approx 2.00$) and the total width of the split signal (see Theory, and ref 52). It is also noted that mixed valence oxo/carboxylato bridged $Mn^{III}Mn^{IV}$ dimers exhibit antiferromagnetic exchange coupling of the order of about -100 cm^{-1} (refs 67−70 and references therein). Similarly, the crystallographic study of Högbom et al.[71] disfavors assigning the oxidation state of the metallocofactor to $Mn^{III}Mn^{II}$. In this earlier work, a purified apo-R2 subunit (*E. coli*) was loaded with Mn^{II} and oxidized to the $Mn^{II}Mn^{III}$ state via the exogenous addition of H_2O_2. This earlier structure is significantly different from the metallocofactor seen in R2F from *C. ammoniagenes* although the two metals have virtually the same co-ordination environment. In particular: (a) the Mn−Mn distance of 3.4 Å is 0.1 Å longer for the $Mn^{II}Mn^{III}$ dimer as compared to the Mn dimer seen in the R2F subunit; and (b) the Mn dimer lacks a μ-oxo bridge. The oxygen ligand to Mn_B is assigned as a monodentate water ligand. The bridging unit instead involves one of the terminal oxygens of a nearby glutamate residue. Thus, a $Mn^{II}Mn^{III}$ dimer as described by Högbom et al.[71] lies between the reduced $Mn^{II}Mn^{II}$ (Figure 6C) and the putative $Mn^{III}Mn^{III}$ structures (Figure 6B).

(iii) The $Mn^{IV}Mn^{IV}$ configuration is a plausible model based on the simple arguments above. However it does not as readily explain the structure or the temperature dependence of the 'split-tyrosyl radical' signal as do the $Mn^{III}Mn^{III}$ simulations (see Figures 9 and 10). It is noted that a $Mn^{IV}Mn^{IV}$ metallocofactor cannot be excluded based solely on the structural data presented. Some synthetic $Mn^{IV}Mn^{IV}$ analogues are likely to exhibit the same structural properties observed here for the metalloradical cofactor of R2F. Structural data have been reported for bis-μ-oxo-$Mn^{IV}Mn^{IV}$ complexes.[68] They generally have short Mn−Mn distances (2.5−2.9 Å), Mn−O−Mn bond angles between 91−102° and are strongly antiferromagnetically coupled (about -100 cm^{-1}) (ref 68 and references therein). A closer structural mimic of the metallocofactor of R2F lacks one of the μ-oxo linkages and instead has a carboxylato bridge. Unfortunately, there are no crystallographic data for μ-oxo-(mono/bis)μ-carboxylato $Mn^{IV}Mn^{IV}$ complexes in the current literature. However, it is noted though that $Mn^{III}Mn^{IV}$ to $Mn^{IV}Mn^{IV}$ conversion is electrochemically reversible for this structural motif,[67] suggesting the ligand environment is nominally the same for both oxidation states. An example of this μ-oxo-(mono/bis)μ-carboxylato $Mn^{III}Mn^{IV}$ complex is $LMn^{III}(\mu\text{-O})(\mu\text{-}CH_3CO_2)_2Mn^{IV}$ (L = *N*,*N*′,*N*″′-trimethyl-1,4,7-triazacyclononane).[72] It has a Mn−Mn separation of ∼3.2 Å, Mn−O bond length of ∼1.8−1.9 Å and Mn−O−Mn bond length of ∼120°. These bond lengths are approximately those seen for the metallocofactor of R2F (see results) albeit slightly shorter.

(iv) In contrast, the $Mn^{III}Mn^{III}$ configuration is consistent with all crystallographic and spectroscopic data. The best mimic of the Mn core structure seen in R2F are μ-oxo-(mono/bis)μ-carboxylato $Mn^{III}Mn^{III}$ complexes, which share the same structural and physical characteristics (ref 68 and references

(67) Wieghardt, K.; Bossek, U.; Nuber, B.; Weiss, J.; Bonvoisin, J.; Corbella, M.; Vitols, S. E.; Girerd, J. J. *J. Am. Chem. Soc.* **1988**, *110*, 7398–7411.
(68) Mukhopadhyay, S.; Mandal, S. K.; Bhaduri, S.; Armstrong, W. H. *Chem. Rev.* **2004**, *104*, 3981–4026.
(69) Schäfer, K. O.; Bittl, R.; Lendzian, F.; Barynin, V.; Weyhermüller, T.; Wieghardt, K.; Lubitz, W. *J. Phys. Chem. B* **2003**, *107*, 1242–1250.
(70) Schäfer, K.-O.; Bittl, R.; Zweygart, W.; Lendzian, F.; Haselhorst, G.; Weyhermüller, T.; Wieghardt, K.; Lubitz, W. *J. Am. Chem. Soc.* **1998**, *120*, 13104–13120.
(71) Högbom, M.; Andersson, M. E.; Nordlund, P. *J. Biol. Inorg. Chem.* **2001**, *6*, 315–323.
(72) Wieghardt, K.; Bossek, U.; Bonvoisin, J.; Beauvillain, P.; Girerd, J. J.; Nuber, B.; Weiss, J.; Heinze, J. *Angew. Chem., Int. Ed. Engl.* **1986**, *25*, 1030–1031.

therein). They generally have Mn−Mn distances of ∼3.3 Å, Mn−O−Mn bond angles between 120−125° and exhibit weak Mn−Mn couplings (<10 cm^{-1}), favoring the ferromagnetic regime.[68] These values closely match the crystallographic data and fitted Mn−Mn exchange coupling seen for the R2F metalloradical cofactor of *C. ammoniagenes* studied here: The Mn−Mn distance of the metalloradical cofactor is 3.3 Å, the Mn−O−Mn bond angle is ∼120° and the estimated exchange coupling is ∼1 cm^{-1}.

It is noted that other synthetic $Mn^{III}Mn^{III}$ complexes involving biologically relevant ligands, do not in general show the same structural features.[68] The Mn−Mn coupling is strongly influenced by the bridging ligands between the two Mn ions. Both ferromagnetic and antiferromagnetic pathways exist in μ-oxo-bridged Mn complexes and the net coupling observed is dominantly dependent on the Mn−O−Mn bond angle (for full discussion see[67,73]). Bis-μ-oxo-$Mn^{III}Mn^{III}$ complexes typically have a Mn−Mn distance of ∼2.7 Å, Mn−O−Mn bond angles of 92−95° and show strong antiferromagnetic coupling (−100 cm^{-1}) (ref 68 and references therein). Similarly, linear (∼180°) Mn−O−Mn bridged complexes [Mn_2O(5-NO_2saldien)$_2$, etc], have a longer Mn−Mn distance (∼3.5 Å) and display large antiferromagnetic coupling between the two Mn centers (J = −120 cm^{-1}).[74] The μ-oxo-(mono/bis)μ-carboxylato $Mn^{III}Mn^{III}$ complexes, as seen in R2F, represent a midpoint between these two limiting regimes. As the Mn−Mn bond length and Mn−O−Mn bond angle, seen for the bis-μ-oxo complexes increases, the ferromagnetic coupling between the two Mn increases to the extent that it approaches or becomes comparable to the antiferromagnetic pathway. It is in this range that the μ-oxo-(mono/bis)μ-carboxylato $Mn^{III}Mn^{III}$ complexes are found (see[67,73]). A further increase in the Mn−Mn distance and bond angle then reduced the ferromagnetic pathway contribution such that linear complexes exhibits similar properties that were seen for the bis-μ-oxo complexes. The balancing of the ferromagnetic and antiferromagnetic bonding pathways seen for μ-oxo-(mono/bis)μ-carboxylato $Mn^{III}Mn^{III}$ complexes should tune the redox chemistry. This could potentially stabilize the tyrosyl radical of the metalloradical cofactor, or alter the chemistry of higher valence states that would be involved in cofactor assembly.

Earlier ICP-MS and X-/Q-band EPR measurements had suggested that the metal site may contain a mononuclear Mn^{II} cluster.[25] Within the model presented in the current study, a Mn^{II} signal is probably reporting on a subfraction of R2F subunits that: (i) did not fully assembly an active metalloradical ($Mn^{III}Mn^{III}$) complex, the metal site may contain either one or two bound Mn^{II}; or (ii) contain nonspecifically bound Mn^{II} attached to the protein surface. As Mn^{II} ($S = {}^5/_2$) is a d^5 metal ion, it typically displays small zero-field splitting (a few 100 MHz) in ligand environments found in biological systems. As a consequence, it often appears as a structured signal, with six sharp lines separated by ∼8 mT, centered at $g \approx 2$. These properties make it readily detectable using EPR. Thus only a small concentration of Mn^{II} needs to be present to observe a large signal.

The $Mn^{III}Mn^{III}$ (quenched radical) state of the R2F subunit, unlike Mn^{II}, is likely to be either invisible at low microwave frequencies (X- or Q-band) or sufficiently broad such that it would be difficult to identify outside of instrumental drift. The calculated simulation parameters for the fine structure tensors of both Mn are large ($D \approx 0.5$ cm^{-1}, $E/D > 0.1$), i.e. of the order of the microwave quanta at X and Q-band. No EPR signal would be expected to be observed using either perpendicular or parallel microwave polarizations for a $Mn^{III}Mn^{III}$ species using this parameter set. Thus we only observe the Mn dimer signal via its coupling with the tyrosine radical. It is also noted that as the coupling between the tyrosyl radical and $Mn^{III}Mn^{III}$ dimer is small, the 'metal signal', transitions that are dominantly Mn in character, should be approximately the same regardless of whether it is coupled to the tyrosyl radical or not.

5.3. Structural Similarities of RNR from *C. ammoniagenes* and *E. coli* (classes Ia and Ib). The Mn metalloradical cofactor of the R2F subunit obtained from *C. ammoniagenes* bears a strong resemblance to the corresponding diferric complex seen in class Ia RNR of *E. coli* (Fe-R2); the only obvious difference is that nature has chosen a different metal for the same catalytic function. The evidence for this is 4-fold: i) Earlier work, using UV/vis absorption spectroscopy, demonstrated that a tyrosyl radical is observed in *C. ammoniagenes*[28,75] and sequence alignment suggest that the tyrosine Y115 of the *C. ammoniagenes* NrdF[16] corresponds to the Y122 harboring the organic radical in *E. coli* Fe-R2[2]. ii) The crystal structure of the Mn containing, metalloradical cofactor is highly similar to the metal site of *E. coli* Fe-R2. The metal−metal distance is the same, the ligand field is virtually identical, and the tyrosine is nominally in the same position in both R2F subunits. Importantly, the structure shows that the two Mn centers of *C. ammoniagenes* are bridged by nonresidue derived oxygen(s), as seen for the Fe-R2 subunit of *E. coli*, which is known in the latter to form from the reaction of the reduced ferrous complex ($Fe^{II}Fe^{II}$) with O_2.[76] iii) Multifrequency EPR measurements and modeling demonstrate the R2F subunit contains a stable redox active tyrosyl, located near (∼8 Å) an exchange coupled Mn dimer and support the assignment of the oxidation state of this dimer to $Mn^{III}Mn^{III}$, the same that is seen for the Fe-R2 subunit (active/met state) of *E. coli* ($Fe^{III}Fe^{III}Y^{\bullet}$).[2,5,76] It is noted that the two Fe^{III} centers of the Fe-R2 metalloradical cofactor are strongly antiferromagnetically coupled. The ground state of the $Fe^{III}Fe^{III}$ spin manifold is diamagnetic ($S = 0$) and thus an unperturbed tyrosyl radical signal is observed albeit with altered relaxation properties. The $Mn^{III}Mn^{III}Y^{\bullet}$ metalloradical cofactor signal is unique with regard to the field of RNR research to date.

5.4. Manganese and Iron Chemistry in Enzymatic Function. Several enzymes have been identified that use Fe or Mn interchangeably. In particular the oxidoreductase enzyme, superoxide dismutase (SOD), which catalyzes the dismutation of superoxide to O_2 and hydrogen peroxide, has evolved both monomeric Fe and Mn forms.[77] The catalytic site of these enzymes, regardless of the identity of the metal, contains a metal center ligated by three histidine residues and an asparate residue and this metallocofactor passes through the same redox states during its catalytic cycle.

(73) Hotzelmann, R.; Wieghardt, K.; Floerke, U.; Haupt, H. J.; Weatherburn, D. C.; Bonvoisin, J.; Blondin, G.; Girerd, J. J. *J. Am. Chem. Soc.* **1992**, *114*, 1681–1696.
(74) Kipke, C. A.; Scott, M. J.; Gohdes, J. W.; Armstrong, W. H. *Inorg. Chem.* **1990**, *29*, 2193–2194.
(75) Barckhausen, O. Doctoral Thesis, Universität Hannover, 2004.
(76) Atkin, C. L.; Thelander, L.; Reichard, P.; Lang, G. *J. Biol. Chem.* **1973**, *248*, 7464–7472.
(77) Meier, B.; Barra, D.; Bossa, F.; Calabrese, L.; Rotilio, G. *J. Biol. Chem.* **1982**, *257*, 13977–13980.

$$M^{III} - SOD + O_2^{\bullet -} \rightarrow M^{II} - SOD + O_2$$
$$M^{II} - SOD + O_2^{\bullet -} + 2H^+ \rightarrow M^{III} - SOD + H_2O_2$$

where M = Fe or Mn.

Another example of Fe and Mn cofactors that facilitate the same catalytic reaction are those found in the catalase enzymes, which catalyze the dismutation of hydrogen peroxide (H_2O_2) to O_2 and H_2O. Nature has independently evolved two types of catalases that contain either a heme Fe[78] or a dinuclear Mn cofactor.[36] It is thus not surprising that the same metal variation is seen in RNR.

Metalloradical cofactor formation in Fe containing class Ia RNR occurs via the reduction of O_2 and is thought to involve a peroxo-bridged di-iron intermediate with maximum oxidation state (Fe^{IV}).[79,80] A dimanganese complex should be able to move through a similar redox pathway. However, the $Mn^{II}Mn^{II}$ complex is unlikely to react with O_2 directly. The isolated apo-R2F protein sourced from *C. ammoniagenes* cannot be reactivated using Mn in the presence of O_2; while the protein binds Mn^{II}, no subsequent redox reaction takes place i.e. a tyrosyl radical is not observed.[26,50] Interestingly, the hydroxyrea quenched R2F protein can be reactivated by the addition of H_2O_2 (and a mediator), see Results 4.1. In this reaction the quenched Mn-cofactor, presumably ($Mn^{III}Mn^{III}Y$) is oxidized to a higher valence state ($Mn^{III}Mn^{IV}$, $Mn^{IV}Mn^{IV}$) both of which are of sufficient potential to oxidize the nearby Y115. It is presently not clear if the same conditions, the addition of H_2O_2 etc., can be used to reactivate the apo-R2F protein in the presence of Mn. This would require a precursory step, the oxidation of the bound $Mn^{II}Mn^{II}$ state to $Mn^{III}Mn^{III}$ as seen for the manganese catalase, which contains a $Mn^{II}Mn^{II}$ cofactor in its reduced state. Our reactivation result is similar to recent observations of Cotruvo and Stubbe,[32] performed *in vitro* using *E. coli* class Ib. They have identified an unusual flavodoxin (NrdI) that may be involved in metalloradical cofactor biosynthesis. They suggest its function may resemble that of flavoprotein oxidases, which catalyze H_2O_2 production from O_2 and thus supply the reduced metallocofactor with peroxide species *in vivo* (H_2O_2, HO_2^- etc).[32] The same subunit (NrdI) has also been identified in *C. ammoniagenes*, and may be common to all class Ib RNRs.[32]

5.5. Proposal for the Mechanism for the Metalloradical Cofactor ($Mn^{III}Mn^{III}Y^{\bullet}$) Generation. A possible mechanistic pathway for Mn metalloradical cofactor assembly has been proposed by Cotruvo and Stubbe[32] and involves two discrete oxidation steps using H_2O_2,/HO_2^-.[81] The first step oxidizes the $Mn^{II}Mn^{II}$ dimer to $Mn^{III}Mn^{III}$ and resembles initially the Mn catalase H_2O_2 dismutation reaction mechanism.[34–36] The second step generates the 'intermediate X', a di-μ-oxo-bridged $Mn^{III}Mn^{IV}$ or $Mn^{IV}Mn^{IV}$ dimer,[82,83] with sufficient oxidizing power to extract an electron from the tyrosine Y115, as seen in di-iron class Ia type RNRs.[79,80] Our crystallographic and EPR data are broadly consistent with this reaction pathway and provides further details as to how protein conformational changes at the dimetal site direct the reaction mechanism, disfavoring alternate pathways i.e. H_2O_2 dismutation. Pathway selectivity appears to be governed by two carboxylate residues, the glutamate E202 and the aspartate D77.

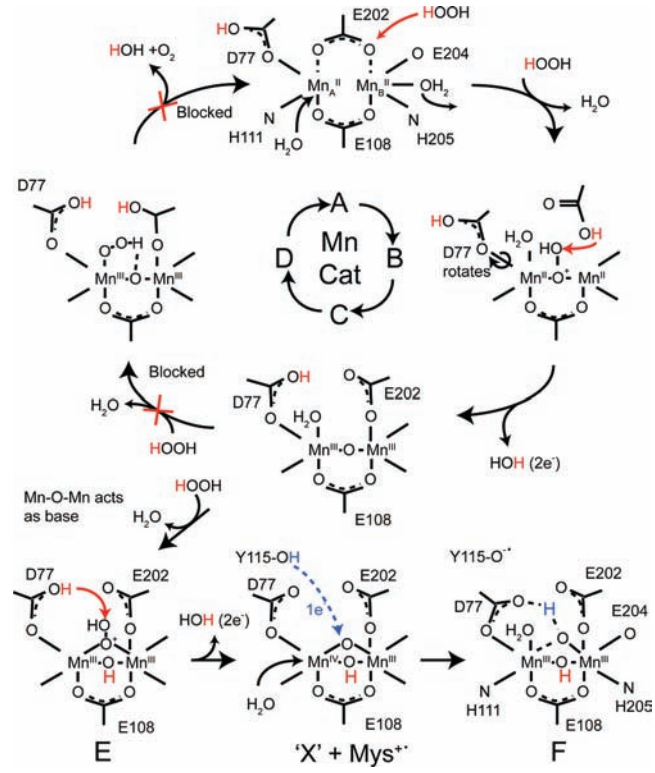

Figure 13. Proposed assembly pathway of the dimanganese metalloradical cofactor of R2F obtained from *C. ammoniagenes*. Structures A, B, C, and D correspond to the catalytic steps of the Mn-catalase H_2O_2 dismutation reaction. Structures E, X and F, correspond to the alternate pathway used to assemble the reactive 'intermediate X' that has a sufficient oxidizing potential to extract an electron from Y115. Pathway selectivity is governed by rotation of a glutamate residue (E202) that acts as an intermolecular base. Red denotes H_2O_2 proton movement; blue denotes Y115−H proton movement. For details see text.

It is first noted that the reduced ($Mn^{II}Mn^{II}$) R2F subunit of *C ammoniagenes* and of *E. coli* (Ib) is very similar to that of Mn catalase (Mn-Cat).[36] The ligand field of the two Mn centers in Mn-Cat contains only glutamates and histidines. An important structural feature is a glutamate residue that acts as an intermolecular base. An analogous glutamate residue (E202) is present in the reduced Mn-R2F metallocofactor; it caps the dimanganese cluster (Figure 6C, Figure 13A). The proposed reaction pathway for metalloradical cofactor assembly initially proceeds along the same mechanism as Mn-Cat (Figure 13A-C). H_2O_2 displaces a water ligand at the distal Mn (to the tyrosine Y115, Mn_B) forming a bridging hydroxoperoxide between the two Mn ions and protonating the E202. Subsequent protonation of the bridging peroxide species leads to two electron oxidation of the $Mn^{II}Mn^{II}$ complex and water release and results in a μ-oxo-bridged $Mn^{III}Mn^{III}$ complex termed here intermediate C (Figure 13C).

(78) Vainshtein, B. K.; Melik-Adamyan, W. R.; Barynin, V. V.; Vagin, A. A.; Grebenko, A. I.; Borisov, V. V.; Bartels, K. S.; Fita, I.; Rossmann, M. G. *J. Mol. Biol.* **1986**, *188*, 49–61.
(79) Burdi, D.; Willems, J.-P.; Riggs-Gelasco, P.; Antholine, W. E.; Stubbe, J.; Hoffman, B. M. *J. Am. Chem. Soc.* **1998**, *120*, 12910–12919.
(80) Willems, J.-P.; Lee, H.-I.; Burdi, D.; Doan, P. E.; Stubbe, J.; Hoffman, B. M. *J. Am. Chem. Soc.* **1997**, *119*, 9816–9824.
(81) Cotruvo and Stubbe suggest the likely oxidant for cofactor assembly is HO_2^- instead of H_2O_2. In the discussion of the metalloradical cofactor assembly we do not distinguish between the two species, all mechanistic arguments are equally valid for either reactive oxygen species.
(82) Sheats, J. E.; Czernuszewicz, R. S.; Dismukes, G. C.; Rheingold, A. L.; Petrouleas, V.; Stubbe, J.; Armstrong, W. H.; Beer, R. H.; Lippard, S. J. *J. Am. Chem. Soc.* **1987**, *109*, 1435–1444.
(83) Wieghardt, K.; Bossek, U.; Ventur, D.; Weiss, J. *J. Chem. Soc., Chem. Commun.* **1985**, 347–349.

If we assume the crystal structure of the metalloradical cofactor ($Mn^{III}Mn^{III}Y^{\bullet}$, Figure 6B) bears a resemblance to intermediate C (Figure 13C), we would suspect two important structural changes have occurred in the surrounding protein matrix: (i) the E202 has been displaced as a bridging bidentate ligand. It now appears as a monodentate carboxylate bound to the distal manganese Mn_B, with 4 Å separation to the proximal Mn_A; and (ii) the D77 has rotated ~180°, bringing its second oxygen into close proximity to the bridging Mn−O−Mn motif (Figure 13C).

The second H_2O_2 is thought to displace a water ligand at an open coordination site on the proximal Mn (Mn_A) as opposed to Mn_B. At this stage in the reaction pathway, E202 can no longer act as a base; it is too far away from the bridging peroxide (Figure 13D). This then prevents the completion of the dismutation cycle, trapping the high valence ($Mn^{III}Mn^{III}$) state. It is instead proposed that the μ-oxo-bridge acts as the proton acceptor (Figure 13E). While the basicity of μ-oxo-bridges between electron-withdrawing Mn ions is likely to be small, it could still act in this manner if we consider that the peroxide species is also ligated to the same metal center. Subsequent protonation of the bridging hydroxoperoxide leads to a second two-electron oxidation and water release (Figure 13X). The resulting $Mn^{IV}Mn^{IV}$ species may only form transiently and rapidly decay to a more stable $Mn^{III}Mn^{IV}$ species by oxidizing a nearby residue as is seen in class I Fe-R2 sourced *E. coli*. In this case, a nearby tryptophan radical is transiently formed during metalloradical cofactor synthesis.[84,85] A tryptophan residue has been identified in R2F from *C. ammoniagenes* in a similar structural position. In our preliminary reactivation experiments, it is suggested that the mediator methyl viologen possibly acts as a one-electron reductant. Regardless, a $Mn^{IV}Mn^{IV}$ or $Mn^{III}Mn^{IV}$ dimer (intermediate X) is of sufficient oxidizing potential to extract an electron from the tyrosine Y115, thus yielding the $Mn^{III}Mn^{III}Y^{\bullet}$ metalloradical cofactor (Figure 13F). It is noted that electron extraction from Y115 may be coupled to proton movement; our EPR measurements are consistent with the Y115 being deprotonated. The tyrosyl radical $Y115\text{-}OH^{+\bullet}$ may protonate the nearby D77, which could in turn participate in a hydrogen-bonding network around the Mn dimer (i.e. with D77). The lengths of the O bridges of the Mn dimer core are more consistent with hydroxo ligands with one bridging the two Mn centers, while the other forms a more asymmetric bridging unit, hydrogen bonded to the nearby D77 residue.

The same organization of residues about the metallocofactor, in particular D77, is not seen for R2F with an assembled $Fe^{III}Fe^{III}$ core in *C. ammoniagenes*.[26] This is perhaps not surprising as the mechanism of complex formation differs; the Fe dimer is assumed to move through an Fe−O−O−Fe peroxide intermediate[86] as opposed to the μ-oxo-bridged Mn dimer proposed above. The D77 residue, as suggested in our reaction mechanism (see above), potentially participates in a concerted proton−electron-coupled transfer and as a consequence, is required to be in close proximity to Mn_A. The same role is not suggested for D77 in Fe cofactor assembly. No reorganization of the D77 is required to assemble the Fe−Fe core, and thus D77 appears in approximately the same position in both the reduced $Fe^{II}Fe^{II}$ state and the oxidized (activated) $Fe^{III}Fe^{III}$ state (see Figure 6D).

5.6. Model for the Incorporation of Fe^{2+} into the Metal Binding Site of RNR from *C. ammoniagenes*. It was noted that the Fe-R2F metalloradical cofactor from *C. ammoniagenes* contains a solvent water molecule in close proximity (3.2 Å) to the tyrosine (Y115).[26] This feature is unique to this Fe-R2F subunit; an additional water molecule other than the water/hydroxo ligand to Mn_A^{III}/Fe_A^{III} has not been observed between the tyrosine and the metal dimer in all other oxidized R2/R2F subunits crystallized so far, including the structurally similar *S. typhimurium* (class Ib).[18] This additional solvent water molecule was considered part of the hydrogen-bonding network about the Y115 in Fe-R2F. The same water molecule is not present in the Mn-bound native system. This is due to the rotation of the phenylalanine residue (Phe172), and thus, this structure more closely resembles the typical environment seen for the redox active tyrosine of class I RNRs. Solvent access to the tyrosyl radical may lead to a faster decay of this radical species and, thus, to a decrease in activity when iron is incorporated into R2F from *C. ammoniagenes*. Preliminary results suggest this is the case in *C. ammoniagenes* and forms part of a continuing study. A similar effect is seen in *mouse* RNR. Its metalloradical cofactor site is more open than the corresponding site in *E. coli* RNR.[87] This appears to correlate with a drop in enzyme activity, i.e. radical stability. Thus incorrect metal binding, while causing minimal localized modification of the enzyme, may lead to global changes in how the protein interacts with the surrounding aqueous medium.

6. Conclusion

The multidisciplinary approach adopted in this study demonstrates conclusively that the native RNR enzyme derived from *C. ammoniagenes* predominantly uses Mn for tyrosyl radical generation and supports the assignment of this RNR to class Ib. The crystal structure of the R2F subunit shows that the metalloradical cofactor contains a bridged oxo/hydroxo Mn dimer in close proximity to a tyrosine (Y115) residue. Concomitant multifrequency EPR measurements confirm these findings and show that the R2F subunit contains a stable redox active tyrosyl radical, located near an exchange coupled Mn dimer (~8 Å), and support the assignment of the oxidation state of this dimer to $Mn^{III}Mn^{III}$ [51], the same that is seen for the Fe-R2 subunit (active/met state) of *E. coli*.[2,5,76]

A $Mn^{III}Mn^{III}$ metallocofactor is consistent with data from model Mn dimer complexes. The best mimic of the manganese core structure seen in R2F are μ-oxo-(mono/bis)μ-carboxylato $Mn^{III}Mn^{III}$ complexes, which share the same structural and physical characteristics (ref 68 and references therein). The μ-oxo-(mono/bis)μ-carboxylato $Mn^{III}Mn^{III}$ motif generally displays very small metal−metal exchange couplings. Here the antiferromagnetic and ferromagnetic coupling pathways effectively cancel each other; this structure type results in the minimum coupling seen between the two Mn^{III} centers. It is unclear why an effectively decoupled Mn dimer is required for tyrosyl radical generation or stabilization.

(84) Baldwin, J.; Krebs, C.; Ley, B. A.; Edmondson, D. E.; Huynh, B. H.; Bollinger, J. M. *J. Am. Chem. Soc.* **2000**, *122*, 12195–12206.
(85) Pötsch, S.; Lendzian, F.; Ingemarson, R.; Hörnberg, A.; Thelander, L.; Lubitz, W.; Lassmann, G.; Gräslund, A. *J. Biol. Chem.* **1999**, *274*, 17696–17704.
(86) Yun, D.; Garcia-Serres, R.; Chicalese, B. M.; An, Y. H.; Huynh, B. H.; Bollinger, J. M. *Biochemistry* **2007**, *46*, 1925–1932.
(87) Kauppi, B.; Nielsen, B. B.; Ramaswamy, S.; Larsen, I. K.; Thelander, K.; Thelander, L.; Eklund, H. *J. Mol. Biol.* **1996**, *262*, 706–720.

A mechanistic pathway for Mn metalloradical cofactor formation involving two discrete oxidation steps using H_2O_2/HO_2^- has been proposed. The initial step oxidizes the $Mn^{II}Mn^{II}$ dimer to $Mn^{III}Mn^{III}$ and resembles the first part of the Mn catalase H_2O_2 dismutation reaction mechanism.[34–36] The second step generates the 'intermediate X', a di-μ-oxo-bridged $Mn^{III}Mn^{IV}$ or $Mn^{IV}Mn^{IV}$ dimer, with sufficient oxidizing power to extract an electron from the tyrosine Y115,[82,83] as seen in di-iron class Ia type RNRs.[79,80] A comparison between our crystal structure of the active Mn-R2F subunit and earlier inactive structures that contain a $Mn^{II}Mn^{II}$ dimer provides further details as to how protein conformational changes at the dimetal site direct the reaction mechanism, disfavoring the completion of the H_2O_2 dismutation cycle, and allow the formation of a high-valence Mn state. Pathway selectivity appears to be governed by two carboxylate residues in the first coordination sphere, the glutamate E202 and the aspartate D77.

These new results in *C. ammoniagenes* in conjunction with the recent report of Cotruvo and Stubbe,[32] suggest that a Mn metalloradical cofactor may be ubiquitous in class Ib RNRs. Thus, the structure and mechanism of assembly presented here for the metalloradical cofactor of *C. ammoniagenes* may be representative of the native R2F subunit seem in all class Ib RNRs.

Protein Data Bank Accession Numbers

The coordinates and structure factor have been deposited in the PDB with accession number, 3MJO.

Acknowledgment. We thank Olaf Barckhausen (University of Hannover), Antonio Pierik (University of Marburg), Thomas Weyhermueller (MPI Mülheim), and Gudrun Klihm (MPI Mülheim) for their help and advice during the preparation of this manuscript. We also acknowledge the important contribution of our former colleague Peter Paul Schmidt (MPI Mülheim), who passed away before its completion. We dedicate this manuscript to his memory. We thank the staff of the beamline BL41XU at SPring-8 (Hyogo, Japan) and the beamline BL14.2 at BESSYII (Berlin, Germany) for their assistance during the data collection. This work was supported by the Max-Planck-Gesellschaft.

Supporting Information Available: Additional XRF data, additional X-band and high-field simulations, figures detailing solvent access channels, specific activities of selected RNRs, collated literature **g**-tensor data for tyrosyl radicals, and the complete authors list of ref 30. This material is available free of charge via the Internet at http://pubs.acs.org.

JA1036995